

# **FEM modeling of plastic flow and strain-induced phase transformation in BN under high pressure and large shear in a rotational diamond anvil cell**

Biao Feng,<sup>1</sup> Valery I. Levitas,<sup>2,3\*</sup> and Wanghui Li<sup>1</sup>

1) *Theoretical Division, Los Alamos National Laboratory, Los Alamos, New Mexico 87545, USA*

2) *Departments of Aerospace Engineering, Mechanical Engineering, and Material Science and Engineering, Iowa State University, Ames, Iowa 50011, USA*

3) *Ames Laboratory, Division of Materials Science and Engineering, Ames, Iowa 50011, USA*

## **Abstract**

Combined three-dimensional plastic flow and strain-induced phase transformation (PT) in boron nitride (BN) under high pressure and large shear in a rotational diamond anvil cell (rotational DAC or RDAC) are investigated. Geometrically nonlinear frameworks including finite elastic, transformational, and plastic deformations and finite element method (FEM) are utilized. Quantitative information is obtained on the evolutions of the stress tensor, plastic strain, volume fraction of phases in the entire sample, and slip-cohesion transitions, all during torsion under a fixed compressive load in RDAC. The effects of the applied compressive stress and the sample radius on PT and plastic flow are discussed. In comparison with DAC, the same amount of the high-pressure phase can be obtained at a much lower pressure in RDAC, which reduces the required force and the risk of diamond fracture. Also, RDAC has a potential to complete PT during torsion under pressure close to the minimum possible. A quasi-homogeneous pressure can be obtained in a transforming sample in RDAC under a proper choice of properties and parameters of a gasket. A number of experimental phenomena, including the pressure self-multiplication and quasi-homogeneous pressures in DAC and RDAC, are reproduced and interpreted. The simulation results provide a significant insight into coupled PTs and plastic flow in material in RDAC, and are important for the optimum design of experiments and the extraction of material parameters for PT, as well as for the optimization and control of PTs by the variation of various parameters.

---

\* Corresponding author.

Emails: [vlevitas@iastate.edu](mailto:vlevitas@iastate.edu) (Valery Levitas); [fengbiao11@gmail.com](mailto:fengbiao11@gmail.com) (Biao Feng); [liwanghui9@gmail.com](mailto:liwanghui9@gmail.com) (Wanghui Li)

**Keywords:** Elastoplasticity, Strain-induced phase transformation, High pressure, Plastic shear, Rotational Diamond anvil cell, Large deformation

## 1. Introduction

In the field of high-pressure research, static high pressures are routinely generated by compressing a thin sample in a diamond anvil cell (DAC). Transparent diamonds allow an *in situ* study of phase transformations (PTs) under high pressure by using advanced diagnostics such as optical, Raman, and x-ray techniques (Dias/ and Silvera, 2017; Dubrovinsky et al., 2012 and 2015; Hemley et al., 1997; Ji et al., 2012). Within a liquid medium, the sample is subjected to a hydrostatic pressure, PTs are pressure-induced, and high-pressure phases nucleate at the preexisting defects. Without a hydrostatic medium, the sample is subjected to large plastic deformation during the thickness reduction, and PTs are considered as plastic strain-induced under high pressures (Levitas, 2004a, b). They occur by nucleation at new defects (e.g. dislocation pileups and grain boundaries), which are continuously generated during plastic flows. Plastic strain-induced PTs require completely different thermodynamic, kinetic, and experimental treatments than pressure-induced PTs. This is even more pronounced under the superposition of large plastic shear on high pressure by rotating one anvil with respect to another pioneered by Bridgman (1935). Bridgman's study with anvils made of hard alloys and similar but more qualitative later studies in a rotational diamond anvil cell (RDAC) revealed many exciting phenomena:

- (a) The PT pressure under plastic shear is reduced by a factor of 2-10 in comparison with the PT pressure under the hydrostatic condition (Alexandrova et al., 1993; Blank et al., 1984 and 1993; Novikov et al., 1999; Levitas et al., 2006; Ji et al., 2012; Blank and Estrin, 2014). For example, the highly disordered nanocrystalline hBN can transform into wBN at 6.7 GPa with severe plastic deformation, whereas wBN was not obtained even at pressures up to 52.8 GPa under quasi-hydrostatic conditions (Ji et al., 2012).
- (b) Plastic deformation promotes the formation of novel phases that would not appear without shear (Blank and Estrin, 2014, Novikov et al., 1999, Levitas et al., 2012). For example, a high-density amorphous phase of SiC is obtained under 30 GPa with large plastic straining, while amorphization did not occur even at 135 GPa under hydrostatic conditions (Levitas et al., 2012).

- (c) A reversible PT under the hydrostatic condition is substituted by an irreversible one with plastic shear (Blank and Dubitsky, 1995; Levitas et al. 2006).
- (d) Plastic shear leads to a reduction (up to zero) in the pressure hysteresis (Blank et al., 1984).
- (e) PTs are of the fast plastic strain-controlled kinetics, in which strain instead of time plays the role of a time-like parameter (Blank and Estrin, 2014, Novikov et al., 1999, Levitas et al., 2006).

Similar experimental results for strain-induced PTs were obtained under lower pressures with the anvils made of hard alloys (Zhilyaev et al., 2010; Edalati et al., 2009), e.g. for PTs in Zr and Ti; see review and analysis in Edalati and Horita (2016). Pure Zr was processed by high-pressure torsion in the pressure range of 1-40 GPa to study the  $\alpha$ -to- $\omega$  PT. It was found that the amount of the  $\omega$  phase increases with plastic straining at pressure above 4 GPa until the saturation occurs, and plastic straining enhances the stability of the  $\omega$  phase of Zr (Edalati et al, 2009). Under high-pressure torsion, the  $\omega$  phase of Zr was obtained at 2.2 GPa in Zilbershtein et al. (1975). Srinivasarao et al. (2011) studied the  $\alpha$  to  $\omega$  plus  $\beta$  transformation in commercially pure zirconium by high-pressure torsion and found that the transformation is orientation-dependent and can be triggered without any applied shear at 1 GPa when the compressive loading is perpendicular to the  $c$ -axis. For the  $\alpha$ -to- $\omega$  plus  $\beta$  transformation in Zr, the transformation pressure can be significantly reduced with large plastic deformation by using an unconstrained high-pressure torsion in comparison with the constrained one (Zhilyaev et al., 2010). Similarly, the shear deformation under high-pressure torsion reduces the transformation pressure in the  $\alpha$ -to- $\omega$  PT in Ti and stabilizes the  $\omega$  phase, which was reported in Zilbershtein et al., 1975; Kilmametov et al., 2007; Todaka et al., 2008. In addition, it was observed experimentally that both the addition of Nb and plastic shear can cause a significant reduction in the transformation pressure in Zr (Zhilyaev et al., 2011). Root et al. (2003) found that the zirconium hydride phase transformation in Zr-2.5Nb is strongly dependent of the concentration of hydrogen and temperature. Strong effects of grain size on the PTs in Ti (Edalati et al., 2014) and TiO<sub>2</sub> ceramics (Razavi-Khosroshahi et al., 2016) were observed experimentally. Because the pressure was estimated as force per area in the above works with anvils made of hard alloys, significant corrections due to pressure heterogeneity were suggested in Feng and Levitas (2017c) and Feng et al. (2018b). From experiment and simulation, Feng et al. (2018c) found that PT and twinning are strongly strain-rate- and loading-orientation-dependent.

Understanding of the interaction between plasticity and PTs in RDAC is an important fundamental problem of high-pressure material physics and mechanics. Strain-induced PTs in RDAC involve multiscale features, and three-scale mechanochemical theory (at nano-, micro-, and macroscale) is described in Levitas (2004a, b). At the nanoscale, a simple analytical model of nucleation at the tip of the dislocation pile-up (Levitas, 2004a, b) was followed by corresponding phase field simulations (Levitas and Javanbakht, 2014, 2015; Javanbakht and Levitas, 2015 and 2016). It was demonstrated that plastic straining can substitute the thermally- activated nucleation with barrierless nucleation and lead to the reduction of the PT pressure by a factor of 2-10 or possibly more, similar to experiments in Alexandrova et al., 1993; Blank et al., 1984 and 1993; Novikov et al., 1999; Levitas et al., 2006; Ji et al., 2012; Blank and Estrin, 2014. Dislocations as the main type of defects are generated and densely pileup against grain boundaries or other obstacles during plastic deformation, which causes strong concentration of the stress tensor. The stresses can be much higher than those caused by preexisting defects under hydrostatic loading. The resulting local stresses near dislocation pileup- induced stress concentrators may be much higher than the applied pressure and may reach the level required for the nucleation of the high-pressure phase.

However, this approach at the nanoscale cannot be directly utilized in the current study because the sample size in RDAC is several hundred microns. Due to complex phase distribution and highly heterogeneous fields of stress and strain tensors, only the pressure at a contact surface and the average volume fraction of the high-pressure phases along the radius of the sample are experimentally available (Levitas et al., 2006; Blank and Estrin, 2014). Also, the distribution and evolution of plastic strain cannot be directly measured. In addition, the PT is plastic strain-controlled and pressure dependent, and pressure and plastic strain are very heterogeneous in the sample. This causes difficulties in determining the kinetics of the strain-induced PT. Because of these obstacles, there are significant challenges in the study and analysis of strain-induced PTs. The only way to understand and quantitatively characterize the interactions between PT and plasticity under high pressure is to develop materials models and formulate FEM algorithms so that strain-induced PTs in RDAC can be studied numerically and compared with limited existing experiments. In this paper, quantitative information will be obtained on the evolutions of the stress

tensor, the plastic strain, the volume fraction of phases of the entire sample, and slip-cohesion transitions during torsion under a fixed compressive load in RDAC.

FEM modeling has been developed and applied for investigation of the evolution of stresses, strains, and volume fraction of phases in the sample during plastic flow and PTs with an external force growth in DAC (Feng et al., 2013a, 2013b, 2014a; Feng and Levitas, 2017c; Levitas and Zarechnyy, 2010a) and under a fixed compressive force and a large torsion in RDAC (Feng and Levitas, 2016; Feng et al., 2014b, 2018b; Levitas and Zarechnyy, 2010b). However, the modeling and these simulations were based on simplified models in which elastic and transformational strains are assumed to be small and the yield strength is pressure-independent. The small elastic and transformational deformation assumption fails for many materials under high pressure and shear. Specifically, for the hBN-to-wBN PT discussed in this paper, the transformational volumetric strain is 0.3. Therefore, another goal of this paper is to study coupled plastic flow and strain-induced PTs in RDAC in a fully large deformation framework, which has not been done before. The theory considering large deformation in elasticity, plasticity, and PT in DAC was developed recently (Feng and Levitas, 2017a) and will be utilized for our three-dimensional model of RDAC for this purpose.

One of the main challenges in studying strain-induced PT experimentally is the heterogeneous distribution of pressure, which causes difficulty in extracting the minimum PT pressure and kinetics of PT. One more goal of this paper is to achieve the quasi-homogenous pressure at the sample in RDAC and to interpret the experimental phenomena. In addition, the torsion in RDAC is applied under a constant compressive force, and the effect of the compressive force will be studied. Because introduction of a gasket into DACs (DACs includes both DAC and RDAC) is a milestone in the history of DACs (Bassett, 2009), the study of the gasket effect on the PT in RDAC is very important and will be discussed in this paper. The results of this paper will show that control of PTs is possible by varying the geometric parameters of RDAC, the gasket material, and the loading conditions, and that FEM modeling can serve as a tool for optimum design of experiments to lead PTs in the desired directions.

The main goals of this paper are summarized as follows:

- (a) To formulate the large deformation model in RDAC for studying coupled strain-induced PTs and plasticity.

- (b) To understand the material complex response in the extreme condition of high pressure and large plastic deformation, and to obtain quantitative and systematic information on the evolutions of the stress tensor, the plastic strain, the volume fraction of phases of the sample, and slip-cohesion transitions during torsion under a fixed compressive load in RDAC, which are currently not available from experiments.
- (c) To achieve quasi-homogeneous pressure in the sample in RDAC by FEM that helps the extraction of material parameters for PTs in an experiment.
- (d) To compare the differences in DAC and RDAC, possibly obtaining the high-pressure phase with a large volume fraction at the lowest pressure to avoid breaking diamond anvils.
- (e) To study the effects of applied compressive force on the stress, strain, and phase volume fraction distributions and to study the effects of the gasket on PTs in RDAC to obtain the high-pressure phase in a large volume with moderately high pressure.

This paper is organized as follows. In Sec. 2, a complete system of equations and material parameters for the sample, gasket, and diamond anvils are summarized. The geometry and boundary conditions used in RDAC are given in Sec. 3. The simulation results in RDAC will be analyzed and discussed in Sec. 4, which can be decomposed into five subsections. The simulation result for RDAC under a fixed compressive force is discussed in Sec 4.1, and the effect of the applied compressive stress is studied in Sec. 4.2. The effect of the sample radius and the differences in DAC and RDAC are investigated in Sec. 4.3 and Sec 4.4. In Sec 4.5, the quasi-homogenous pressure in the sample is obtained in both RDAC and DAC.

At the outset, let us designate the notations for this paper. The subscripts  $a$  and  $s$  represent the skew-symmetrization and symmetrization, respectively; the subscripts 1 and 2 in elastic and plastic material parameters represent the low-pressure and high-pressure phases, respectively; the superscripts  $t$  and  $-1$  represent the transposition and inverse of a tensor; the subscripts  $e$ ,  $p$ , and  $t$  denote the elastic, plastic, and transformational deformation gradient or strain; and  $\mathbf{I}$  is the second-order unit tensor. The contractions of the second-order tensors over one and two indices are designated as  $\mathbf{A} \cdot \mathbf{B} = \{A_{ij} B_{jk}\}$  and  $\mathbf{A} : \mathbf{B} = \{A_{ij} B_{ji}\}$ , respectively. Similarly, contractions of the fourth-order tensor  $\mathbf{H}$  and second-order tensor  $\mathbf{Q}$  over one and two indices are defined as  $\mathbf{H} \cdot \mathbf{Q} = \{H_{ijkl} Q_{mn}\}$  and  $\mathbf{H} : \mathbf{Q} = \{H_{ijkl} Q_{mk}\}$ .

## 2. A complete system of equations and material parameters for the sample, gasket, and anvil

Feng et al. (2016) formulated a thermodynamically-consistent system of equations for a rhenium (Re) sample and diamond anvil in DAC in the framework of fully large deformation, developed a computational algorithm with an emphasis on the stress iteration and update in FEM simulations, and further numerically reproduced the experimental pressure distribution up to 300 GPa (Hemley et al., 1997). Afterwards, Feng and Levitas (2017a) further extended their model to include combined plastic flow and strain-induced phase transformation in a sample under the loadings of a large deformation and high pressure in DAC, and the constitutive equations in Feng and Levitas (2017a) can be degraded into elastoplastic theory in Feng et al. (2016) by fixing the volume fraction of the high-pressure phase as zero. In this paper, we summarize the complete system of constitutive equations from (Feng et al., 2016 and Feng and Levitas 2017a), and the material parameters for the BN sample, Re gasket, and diamond anvil are the same as in these two references.

### 2.1 General equations for sample and gasket

The general system of equations for coupled plastic flow and plastic strain-induced PT, which is directly applied for the BN sample, is summarized in this section. For the Re gasket, PT does not take place, and we can simply set  $\mathbf{F}_i = \mathbf{I}$  in Eq. (1) and  $k=0$  in kinetic equation (16).

*Kinematics.* The material motion is described by a vector function  $\mathbf{r} = \mathbf{r}(\mathbf{r}_0, t)$ . Here,  $\mathbf{r}$  and  $\mathbf{r}_0$  are the position vectors of material points in the actual configuration  $\Omega$  at time instant  $t$  and in the reference configuration  $\Omega_0$  at the instant  $t_0$ , respectively. The deformation gradient  $\mathbf{F} = \frac{\partial \mathbf{r}}{\partial \mathbf{r}_0}$  is

decomposed into elastic  $\bar{\mathbf{F}}_e$  and inelastic  $\mathbf{F}_i$  contributions:

$$\begin{aligned} \mathbf{F} &= \bar{\mathbf{F}}_e \cdot \mathbf{F}_i = \bar{\mathbf{R}}_e \cdot \bar{\mathbf{U}}_e \cdot \mathbf{R}_i \cdot \mathbf{U}_i = \mathbf{R}_e \cdot \mathbf{U}_e \cdot \mathbf{U}_i = \mathbf{F}_e \cdot \mathbf{U}_i = \mathbf{V}_e \cdot \mathbf{R}_e \cdot \mathbf{U}_i \\ \text{with } \mathbf{R}_e &= \bar{\mathbf{R}}_e \cdot \mathbf{R}_i; \quad \mathbf{U}_e = \mathbf{R}_i^t \cdot \bar{\mathbf{U}}_e \cdot \mathbf{R}_i; \quad \mathbf{F}_e = \mathbf{R}_e \cdot \mathbf{U}_e = \mathbf{V}_e \cdot \mathbf{R}_e, \end{aligned} \quad (1)$$

where inelastic deformation gradient  $\mathbf{F}_i$  includes the plastic and transformational parts;  $\mathbf{U}_e$  (or  $\bar{\mathbf{U}}_e$ ) and  $\mathbf{U}_i$  are symmetric elastic and inelastic right stretch tensors;  $\bar{\mathbf{R}}_e$ ,  $\mathbf{R}_e$ , and  $\mathbf{R}_i$  are the

proper orthogonal rotation tensors; and  $V_e$  is the elastic left stretch tensor. The Lagrangian and Eulerian elastic strain tensors are

$$\mathbf{E}_e = 0.5(\mathbf{U}_e \cdot \mathbf{U}_e - \mathbf{I}); \quad \mathbf{B}_e = 0.5(\mathbf{V}_e \cdot \mathbf{V}_e - \mathbf{I}). \quad (2)$$

The velocity gradient  $\mathbf{l} = \dot{\mathbf{F}} \cdot \mathbf{F}^{-1} = \mathbf{W} + \mathbf{d}$  is decomposed into symmetric  $\mathbf{d} = (\mathbf{l})_s$  and skew-symmetric spin  $\mathbf{W} = (\mathbf{l})_a$  tensors. Differentiating Eq. (1), the following decomposition of the deformation rate  $\mathbf{d}$  can be directly derived (see (Levitas, 1996)):

$$\mathbf{d} = \overset{\nabla}{\mathbf{B}}_e - 2(\mathbf{d} \cdot \mathbf{B}_e)_s + \mathbf{V}_e \cdot \mathbf{D}_i \cdot \mathbf{V}_e \quad \text{with} \quad \mathbf{D}_i = \mathbf{R}_e \cdot (\dot{\mathbf{U}}_i \cdot \mathbf{U}_i^{-1})_s \cdot \mathbf{R}_e^t; \quad \overset{\nabla}{\mathbf{B}}_e = \dot{\mathbf{B}}_e - 2(\mathbf{W} \cdot \mathbf{B}_e)_s, \quad (3)$$

where  $\overset{\nabla}{\mathbf{B}}_e$  is the Jaumann objective time derivative of  $\mathbf{B}_e$ , and  $\mathbf{D}_i$  is the inelastic deformation rate.

$\mathbf{D}_i$  can be decomposed into the plastic  $\mathbf{D}_p$  and transformational  $\mathbf{D}_t$  components:  $\mathbf{D}_i = \mathbf{D}_p + \mathbf{D}_t$ .

The transformational velocity gradient  $\mathbf{D}_t$  is

$$\mathbf{D}_t = (\bar{\varepsilon}_t \mathbf{I} + \boldsymbol{\gamma}_t) \dot{c}; \quad \bar{\varepsilon}_t = \bar{\varepsilon}_{t0} / 3, \quad (4)$$

where  $\dot{c}$  is the rate of the volume fraction of the high-pressure phase in the reference configuration;  $\bar{\varepsilon}_{t0}$  is the volumetric transformational strain and  $\boldsymbol{\gamma}_t$  is the transformational shear strain tensor for complete PT ( $c=1$ ). For simplicity, we assume that, in simulations,  $\mathbf{I} : \boldsymbol{\gamma}_t = 0$ .

The plastic velocity gradient  $\mathbf{D}_p$  has volumetric and deviatoric parts:

$$\mathbf{D}_p = \dot{\varepsilon}_{p0} \mathbf{I} + \boldsymbol{\gamma}; \quad \dot{\varepsilon}_{p0} = \mathbf{I} : \mathbf{D}_p / 3. \quad (5)$$

As usual, the plastic flow is assumed to be incompressible, which leads to  $\dot{\varepsilon}_{p0} = 0$ .

*Nonlinear isotropic elasticity.* The elasticity rule for isotropic materials has the following form (e.g. see Clayton, 2011; Levitas, 1996; Lurie, 1990)

$$\boldsymbol{\sigma} = J^{-1}(2\mathbf{B}_e + \mathbf{I}) \cdot \frac{\partial \Psi}{\partial \mathbf{B}_e}; \quad J = \det \mathbf{F}. \quad (6)$$

Here,  $\boldsymbol{\sigma}$  is the Cauchy stress,  $\det \mathbf{F}$  is the determinant of tensor  $\mathbf{F}$ , and  $\Psi$  is the Helmholtz free energy. To consider large elastic strain, the third-order Murnaghan potential  $\Psi$  is used (Murnaghan, 1951):

$$\Psi(\mathbf{B}_e) = \frac{\lambda_e + 2G}{2} I_1^2 - 2GI_2 + \left( \frac{l+2m}{3} I_1^3 - 2mI_1I_2 + nI_3 \right), \quad (7)$$

in which  $G$ ,  $\lambda_e$ ,  $l$ ,  $m$ , and  $n$  are elastic material parameters, and they depend on the volume fraction  $c$  of the high-pressure phase:

$$G = (1-c)G_1 + cG_2, \quad \lambda_e = (1-c)\lambda_{e1} + c\lambda_{e2}, \quad m = (1-c)m_1 + cm_2, \\ l = (1-c)l_1 + cl_2, \quad \text{and} \quad n = (1-c)n_1 + cn_2. \quad (8)$$

$I_1$ ,  $I_2$ , and  $I_3$  in Eq. (7) are the first, second, and third invariants of the strain tensor  $\mathbf{B}_e$ :

$$I_1 = B_{e_{11}} + B_{e_{22}} + B_{e_{33}}; \quad I_2 = B_{e_{22}}B_{e_{33}} - B_{e_{23}}^2 + B_{e_{11}}B_{e_{33}} - B_{e_{13}}^2 + B_{e_{22}}B_{e_{11}} - B_{e_{12}}^2; \quad I_3 = \det \mathbf{B}_e. \quad (9)$$

Further, the Cauchy stress yields

$$\boldsymbol{\sigma} = J^{-1} (2\mathbf{B}_e + \mathbf{I}) \cdot \left( \lambda_e I_1 \mathbf{I} + 2G\mathbf{B}_e + (lI_1^2 - 2mI_2) \mathbf{I} + n \frac{\partial I_3}{\partial \mathbf{B}_e} + 2mI_1 \mathbf{B}_e \right), \quad (10)$$

$$\text{in which } \frac{\partial I_3}{\partial \mathbf{B}_e} = \begin{pmatrix} B_{e_{22}}B_{e_{33}} - B_{e_{23}}B_{e_{32}} & B_{e_{23}}B_{e_{31}} - B_{e_{33}}B_{e_{21}} & B_{e_{21}}B_{e_{32}} - B_{e_{22}}B_{e_{31}} \\ B_{e_{23}}B_{e_{31}} - B_{e_{33}}B_{e_{21}} & B_{e_{11}}B_{e_{33}} - B_{e_{13}}B_{e_{31}} & B_{e_{12}}B_{e_{31}} - B_{e_{11}}B_{e_{32}} \\ B_{e_{21}}B_{e_{32}} - B_{e_{22}}B_{e_{31}} & B_{e_{12}}B_{e_{31}} - B_{e_{11}}B_{e_{32}} & B_{e_{11}}B_{e_{22}} - B_{e_{12}}B_{e_{21}} \end{pmatrix}.$$

*Flow rule.* The  $J_2$  flow theory is used as follows:

$$\mathbf{n} = \frac{\boldsymbol{\gamma}}{|\boldsymbol{\gamma}|} = \sqrt{3/2} \mathbf{s} / \sigma_y; \quad \varphi = \mathbf{n} : \mathbf{n} - 1 = \sigma_i - \sigma_y(c, p, q) = 0; \quad \sigma_i = \sqrt{3/2} \mathbf{s} : \mathbf{s}. \quad (11)$$

Here  $\mathbf{s}$  is the deviator of the Cauchy stress;  $\sigma_y$  is the yield strength that is a function of the volume fraction of the high-pressure phase  $c$ , pressure  $p$ , and accumulated plastic strain  $q$ ; and  $\sigma_i$  is the von Mises equivalent stress. Then the plastic flow rule is

$$\boldsymbol{\gamma} = \lambda \frac{\mathbf{s}}{\sqrt{\mathbf{s} : \mathbf{s}}}, \quad (12)$$

where  $\lambda \geq 0$  is a scalar function determined from the consistency condition  $\dot{\varphi} = 0$ .

The accumulated plastic strain  $q$  is defined by

$$\dot{q} = (2\boldsymbol{\gamma} : \boldsymbol{\gamma} / 3)^{0.5} = \sqrt{2/3} \lambda. \quad (13)$$

It was shown in Levitas (1996) for more than 60 materials for different material classes (e.g. metals, alloys, oxides, rocks, compacted powders) that, despite the plastic strain-induced anisotropy and history-dependence, above some level of plastic strain  $q > m$  and, for a deformation path without sharp changes in directions (monotonous deformation), the initially isotropic polycrystalline materials are deformed as isotropic and plastic strain history-independent, i.e.  $\sigma_y = \sigma_y(c, p)$ . The linear dependence of yield strength in pressure is accepted:

$$\sigma_y = \sigma_{y_0} + bp, \quad (14)$$

where  $\sigma_{y_0}$  is the yield strength at zero pressure and  $b$  is the material parameter. They depend on the volume fraction of phases:

$$\sigma_{y_0} = (1-c)\sigma_{y_01} + c\sigma_{y_02}; \quad b = (1-c)b_1 + cb_2. \quad (15)$$

*Strain-induced pressure-dependent PT kinetics.* In the micro-scale theory (Levitas, 2004a), strain-induced PTs can be characterized in terms of the pressure-dependent, strain-controlled kinetic equation:

$$\frac{dc}{dq} = k \frac{(1-c)\bar{p}_d H(\bar{p}_d) \frac{\sigma_{y2}}{\sigma_{y1}} - c\bar{p}_r H(\bar{p}_r)}{c + (1-c) \frac{\sigma_{y2}}{\sigma_{y1}}}, \quad (16)$$

Here, the kinetic parameter  $k$  scales the rate of PTs;  $\bar{p}_r = \frac{p - p_\varepsilon^r}{p_h^r - p_\varepsilon^r}$  and  $\bar{p}_d = \frac{p - p_\varepsilon^d}{p_h^d - p_\varepsilon^d}$  are dimensionless characteristic pressures for the reverse and direct PTs; when  $\bar{p}_d$  (or  $\bar{p}_r$ ) is larger than zero, the Heaviside step function  $H(\bar{p}_d)$  (or  $H(\bar{p}_r)$ ) is equal to 1, and otherwise  $H(\bar{p}_d)$  (or  $H(\bar{p}_r)$ ) is zero;  $p_h^d$  and  $p_h^r$  are the pressures for direct and reverse PTs under hydrostatic loading, respectively;  $p_\varepsilon^d$  is the minimum pressure below which direct strain-induced PT to the high-pressure phase does not take place;  $p_\varepsilon^r$  is the maximum pressure above which reverse strain-

induced PT to the low-pressure phase cannot occur; yield strengths yield  $\sigma_{y1} = \sigma_{y01} + b_1 p$  and  $\sigma_{y2} = \sigma_{y02} + b_2 p$ .

Then the transformational deformation rate can be expressed as

$$\mathbf{D}_t = c\bar{\varepsilon}_t \mathbf{I} = A\mathbf{I}\dot{q} = A\mathbf{I}\sqrt{2/3}\lambda; \quad A = k\bar{\varepsilon}_t \frac{(1-c)\bar{p}_d H(\bar{p}_d) \frac{\sigma_{y2}}{\sigma_{y1}} - c\bar{p}_r H(\bar{p}_r)}{c + (1-c) \frac{\sigma_{y2}}{\sigma_{y1}}}. \quad (17)$$

## 2.2 Nonlinear single-crystal elasticity for diamond

The elasticity rule for an anisotropic material, particularly single crystal, is (Clayton, 2011; Levitas, 1996; Lurie, 1990):

$$\boldsymbol{\sigma} = \mathbf{F} \cdot \tilde{\mathbf{T}}(\mathbf{E}) \cdot \mathbf{F}^t / \det \mathbf{F}; \quad \tilde{\mathbf{T}} = \partial \Psi / \partial \mathbf{E}, \quad (18)$$

in which  $\tilde{\mathbf{T}}$  is the second Piola-Kirchhoff stress. Because diamond anvils have no plastic deformation under the loading considered in this paper, the subscript  $e$  is dropped from Eq. (18).

The third-order potential  $\Psi$  for the cubic symmetry for large elastic deformation is:

$$\begin{aligned} \Psi = & 0.5c_{11}(\eta_1^2 + \eta_2^2 + \eta_3^2) + c_{12}(\eta_1\eta_2 + \eta_1\eta_3 + \eta_2\eta_3) + 0.5c_{44}(\eta_4^2 + \eta_5^2 + \eta_6^2) + c_{111}(\eta_1^3 + \eta_2^3 + \eta_3^3) / 6 \\ & + 0.5c_{112}[\eta_1^2(\eta_2 + \eta_3) + \eta_2^2(\eta_1 + \eta_3) + \eta_3^2(\eta_1 + \eta_2)] + c_{123}\eta_1\eta_2\eta_3 + 0.5c_{144}(\eta_1\eta_4^2 + \eta_2\eta_5^2 + \eta_3\eta_6^2) \\ & + 0.5c_{166}[(\eta_2 + \eta_3)\eta_4^2 + (\eta_1 + \eta_3)\eta_5^2 + (\eta_1 + \eta_2)\eta_6^2] + c_{456}\eta_4\eta_5\eta_6, \end{aligned} \quad (19)$$

in which  $\eta_1 = E_{11}$ ,  $\eta_2 = E_{22}$ ,  $\eta_3 = E_{33}$ ,  $\eta_4 = 2E_{23}$ ,  $\eta_5 = 2E_{31}$ , and  $\eta_6 = 2E_{12}$ .

Thus, the second Piola-Kirchhoff stress can be obtained from Eqs. (18) and (19), and two explicit examples for the components are

$$\begin{aligned} \tilde{T}_{11} = \frac{\partial \Psi}{\partial \eta_1} = & c_{11}\eta_1 + c_{12}(\eta_2 + \eta_3) + c_{111}\eta_1^2 / 2 + c_{112}[2\eta_1(\eta_2 + \eta_3) + \eta_2^2 + \eta_3^2] / 2 + c_{123}\eta_2\eta_3 \\ & + c_{144}\eta_4^2 / 2 + c_{166}(\eta_5^2 + \eta_6^2) / 2; \quad \tilde{T}_{12} = \frac{\partial \Psi}{\partial \eta_6} = c_{44}\eta_6 + c_{144}\eta_3\eta_6 + c_{166}(\eta_1 + \eta_2)\eta_6 + c_{456}\eta_4\eta_5. \end{aligned} \quad (20)$$

## 2.3 Material properties

*Re material properties.* Re is widely used as a gasket material in a diamond anvil cell due to its large bulk ( $K$ ) and shear ( $G$ ) moduli and sufficiently high compressive strength (Jeanloz et al., 1991; Manghnan et al., 1974; Vohra et al., 1987), which could retain appreciable sample thickness even at several megabar pressures without any “punch-through” at the edges of the diamond anvils. The equations in Section 2.1 are directly used for a Re gasket by setting  $c=0$  and  $F_t = I$ . Eqs. (4), (16), and (17) for PT should not be used. The following material properties for Re are used in simulation: Elastic constants (Feng et al., 2016; Jeanloz et al., 1991; Manghnan et al., 1974)  $G = 200$  GPa ,  $\lambda_e = 247$  GPa ,  $l = -291$  GPa ,  $m = -662$  GPa , and  $n=0$ , and plastic properties (Feng et al., 2016; Jeanloz et al., 1991)  $\sigma_{y_0} = 8.00$  GPa and  $b = 0.04$ . Used in our recent paper (Feng et al., 2016), such properties produce good correspondence with the experimental pressure distribution (Hemley et al., 1997) at pressures up to 300 GPa.

*BN material properties.* BN has several crystalline forms. Hexagonal hBN is the most stable and soft of these and is widely used as a lubricant and an additive to cosmetic products. The direct solid-solid PT from hBN to wBN can take place in extreme conditions of high pressure. Phase transformation pressure from hBN to wBN strongly increases with increasing degree of two-dimensional disorder or concentration of turbostratic stacking faults. Turbostratic stacking faults are formed in hexagonal or rhombohedral layered crystal structures by relative rotation or displacement of two parts of a lattice in (001) planes to arbitrary positions (Britun and Kurdyumov, 2000). While low-disordered hBN transforms around 10 GPa to wBN (Levitas et al., 2006), wBN cannot be obtained at pressures up to 52.8 GPa under quasi-hydrostatic conditions (Ji et al., 2012). It was found in Ji et al. (2012) that a highly-disordered hBN-to-wBN transformation occurs at the pressure of 6.7 GPa with plastic shear, exhibiting reduction of PT pressure by nearly an order of magnitude. Therefore, here we will model highly-disordered hBN and take  $p_h^d = 55$  GPa and  $p_e^d = 6.7$  GPa . WBN obtained by strain-induced PT from disordered hBN is stable in the atmospheric pressure. Consequently,  $p_e^r$  and  $p_h^r$  are not important parameters, and we can choose  $p_e^r = -3.0$  GPa and  $p_h^r = -6.0$  GPa, which do not participate in our simulation because the minimum pressure is higher than zero. The yield strengths of hBN and wBN depend on material defects, grain sizes, purities, etc., and in this paper, reasonable values are used as  $\sigma_{y_0 2} = 30\sigma_{y_0 1} = 9$  GPa (Wills, 1985) and  $b_1 = b_2 = 0.01$  . During PT, the volume significantly

reduces and volumetric transformation strain  $\bar{\varepsilon}_{t_0} = 0.3$  (Nagakubo et al., 2013; Rumyantsev et al., 2001). The elastic constants for hBN are taken as  $G_1 = 20$  GPa,  $B_1 = 37$  GPa,  $\frac{dG_1}{dp} = 2.5$  GPa, and  $\frac{dB_1}{dp} = 5.6$  GPa (Solozhenko and Elf, 1998); for wBN, we have  $G_2 = 384$  GPa,  $B_2 = 397$  GPa,  $\frac{dG_2}{dp} = 1.0$  GPa, and  $\frac{dB_2}{dp} = 3.7$  GPa (Kim et al., 1996; Saib and Bouarissa, 2009); similar to Feng et al., 2016, with  $n_1 = n_2 = 0$  we can further obtain  $\lambda_{e_2} = 141$  GPa,  $l_2 = -245$  GPa, and  $m_2 = -657$  GPa for wBN and  $\lambda_{e_1} = 24$  GPa,  $l_1 = -35$  GPa, and  $m_1 = -75$  GPa for hBN. Similar to Feng and Levitas, we use  $k=3$  as a reasonable value for the rate of PT.

*Diamond elastic properties.* In this paper, the second-order elastic constants for a diamond anvil are from Nielsen, 1986:  $c_{11} = 1050$  GPa,  $c_{12} = 127$  GPa, and  $c_{44} = 550$  GPa, and the third-order elastic constants are taken from Lang and Gupta, 2011:  $c_{111} = -7603$  GPa,  $c_{123} = -835$  GPa,  $c_{112} = -1909$  GPa,  $c_{144} = 1438$  GPa,  $c_{166} = -3938$  GPa, and  $c_{456} = -2316$  GPa.

### 3. Geometry and boundary conditions in RDAC

The schematic of a RDAC is presented in Fig. 1a, in which the sample (red color) is clamped by two diamond anvils and surrounded by the gasket. The loadings in a RDAC drawn in Fig. 1a are exerted in two consecutive steps: first, the axial normal compressive stress  $\sigma_n$  is applied at the anvil surfaces; second, the top surface of the upper anvil is rotated with a rotation angle  $\varphi$  about the  $z$ -axis by a torque with respect to the bottom surface of the lower anvil, under a constant  $\sigma_n$ . The geometric parameters of RDAC from experiment (Ji et al., 2012; Levitas et al., 2006) are used in our FEM models, and the details are marked in Figs. 1b and 1c. While the geometry of RDAC is axisymmetric, the loading (due to the rotation of the anvil by the torque) is three-dimensional, which is distinct from the two-dimensional model for DAC (Feng and Levitas, 2017a). As stated in Feng et al., 2016, it is reasonable to neglect the material anisotropy for the single-crystal diamond in the circumferential direction but keep anisotropy in the  $rz$  plane. Due to

symmetry, a quarter of RDAC as shown in Fig. 1b is considered in our simulations, which significantly reduces the computation. In the preceding FEM model under megabar pressures (Feng et al., 2016), the bottom contact surface of a diamond anvil with a bevel angle of  $8.5^\circ$  is used, which is consistent with experiment (Hemley et al., 1997). Typically (as in experiment in Ji et al., 2012; Levitas et al., 2006), a flat anvil surface is used instead of an inclined surface at pressures below 50 GPa; see line *CDK* in Fig. 1c. The geometric parameters in the undeformed configuration are given in Fig. 1b for the anvil and Fig. 1c for the sample and gasket. At point *K* at the contact surface between the gasket and anvil in Fig. 1c, a smooth transition with a  $45^\circ$  arc instead of a sharp angle is used to avoid the penetration of the anvil elements into the sample elements.

The boundary conditions for a quarter of RDAC in Fig. 1b are listed below:

- (1) The normal compressive stress  $\sigma_n$  is applied at the top of anvil surface *AB*, and a torque is then applied on surface *AB* to rotate it along the *z*-axis under a constant  $\sigma_n$ .
- (2) Due to symmetry, the radial displacement  $u_r$  and shear stresses  $\tau_{rz}$  and  $\tau_{z\theta}$  are zero at the *z*-axis (i.e. for  $r = 0$ , the line *AC* for the anvil and the line *CF* for the sample).
- (3) At the contact surface of the diamond anvil in contact with the gasket or sample (the surface *CDKG*), the Coulomb friction model is utilized and the Coulomb friction coefficient  $\mu$  is 0.15. Sliding between two contact surfaces can occur when the friction stress  $\tau_f$  reaches  $\mu\sigma_c$ , where  $\sigma_c$  is the normal contact stress.
- (4) At the contact surface between the sample and gasket (the surface *DE*), the cohesion condition is applied and no sliding is allowed.
- (5) At the symmetry plane  $z = 0$  (the plane *FEJ*), the radial shear stresses  $\tau_{rz} = 0$ ; the axial and circumferential displacements  $u_z = u_\phi = 0$ .
- (6) Other surfaces (such as surface *BHG* in Fig. 1b and surface *GIJ* in Fig. 1c) not mentioned above are stress-free surfaces.

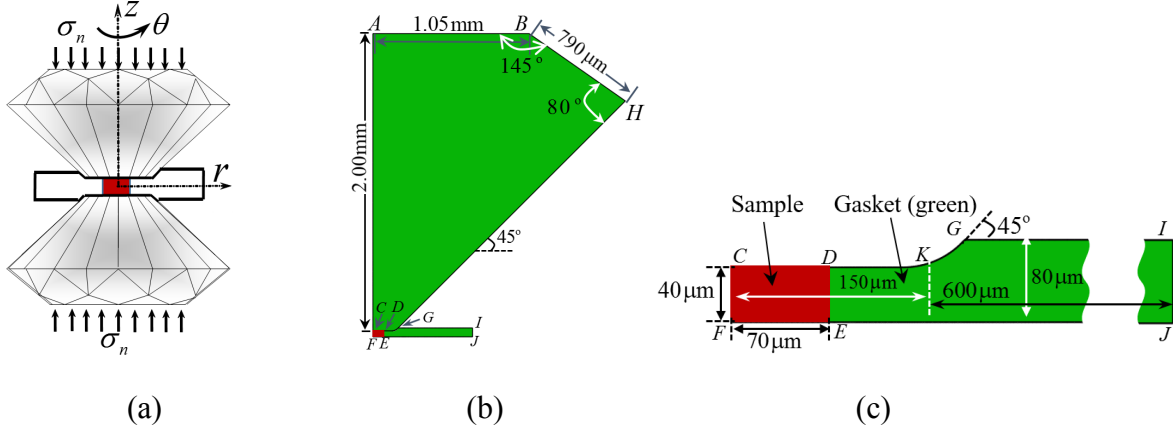


**FIG. 1.** (a) Rotational diamond anvil cell scheme, (b) a quarter of the sample, gasket and anvil in the initial undeformed state and the geometry of a quarter of anvil ( $ABHGDC$ ), and (c) the geometry of a quarter of sample ( $CDEF$ ) and gasket ( $DKGIJE$ ).

Heating due to plastic flow and latent heat of PT, as well as strain-rate effects, can be neglected for loading in RDAC for the following reasons: (a) The compression and torsion process is slow and is often interrupted for producing measurements of X-ray patterns, Raman spectra, and fluorescence of the ruby particles used for measurement of the pressure distribution, and (b) The sample and gasket are thin (10-150 $\mu\text{m}$ ) and are compressed by two diamonds, the best heat conductor.

#### 4. Results and discussions on strain-induced PT in the BN sample in

##### RDAC

The simulation results by FEM on a combined strain-induced PT and plasticity in BN under high pressure and large shear in RDAC are presented and analyzed in this section, which is organized as follows. In Sec. 4.1, we investigate the evolutions and distributions of the stress tensor, plastic strain, phase volume fraction in the sample, and then the deformation of the diamond and the siding of the contact surface between the diamond and sample are discussed, under an increasing rotation angle  $\varphi$  at a fixed compressive stress  $\sigma_n$ . In Sec. 4.2, the effects of the applied compressive stress  $\sigma_n$  in RDAC on the plastic deformation, pressure, and PT are investigated by choosing  $\sigma_n = 0.6, 0.64,$  and  $0.68$  GPa. The effects of the sample radius are studied in Sec. 4.3. In Sec. 4.4, the difference between DAC and RDAC is analyzed and the potential advantages of RDAC are formulated. The experimental results for quasi-homogenous pressure in DAC and

RDAC are reproduced and interpreted in Sec. 4.5. The RDAC geometric parameters are the same as in Fig. 1 for Sec. 4.1, 4.2 and 4.4. There are some slight changes in the geometry of RDAC in Sec. 4.3 and 4.5 from that in Fig. 1; these changes will be introduced in those sections.

#### 4.1 Simulation results for RDAC under a fixed compressive force

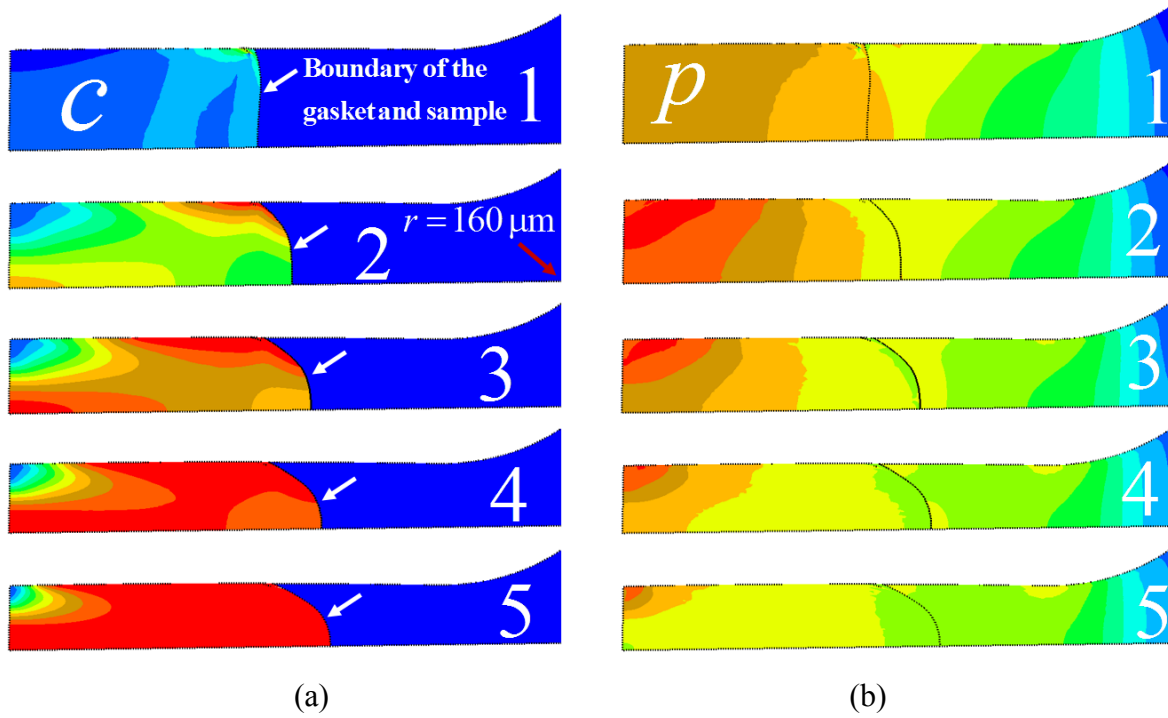
Fig. 2 presents the distributions of the volume fraction of high-pressure phase wBN, pressure, and accumulated plastic strain in the sample and gasket during torsion under a fixed compressive stress  $\sigma_n = 0.64$  GPa. Before torsion with  $\sigma_n = 0.64$  GPa, the volume fraction of wBN is quite small due to a low plastic straining, while the pressure is much higher than the minimum pressure for strain-induced PT,  $p_\varepsilon^d$ . For the strain-induced PT, as long as the pressure is larger than  $p_\varepsilon^d$ , the plastic strain plays the role of a time-like parameter: with increasing plastic strain, PT occurs but without plastic straining PT stops. With the initiation of torsion, the largest amount of wBN is near corner D in Fig. 1d, where the sample, gasket and anvil meet. The second region with larger pressure but a smaller amount of wBN is near center F. A complete PT in the small region near corner D occurs for  $\varphi < 0.2$  and at center F for  $\varphi < 0.5$ . With an increasing rotation angle, the wBN propagates toward each other from these two regions, with the major part of a sample completely transformed at  $\varphi = 1.2$ , except for the very small region near the contact surface at the center of the sample. This non-fully-transformed small region is caused by a small plastic deformation as shown in Fig. 2c. This tendency of PT propagation is very different from that in Feng et al., 2018b, in which PT initiates without a gasket at the center of the sample and propagates from the center to the periphery and from the symmetry plane to the contact surface. Such a large volume fraction of the high-pressure phase shown in Fig. 2a under a large rotation is not possible without using a gasket; see Feng et al., 2018b. Without a strong gasket, pressure is very low at the periphery and material continues to flow into the periphery during compression or torsion. With a gasket, before torsion and for  $\varphi = 1.2$ , Fig. 2b shows that the pressure is quasi-homogeneous throughout the entire sample. The maximum pressure for  $\varphi = 1.2$  is localized at the center of the sample and near the contact surface. While the high pressure intensifies the PT process in this region, the amount of wBN phase is at the minimum because the small plastic strain effect surpasses the effect of the pressure on the PT rate. Consequently, the pattern of the wBN volume

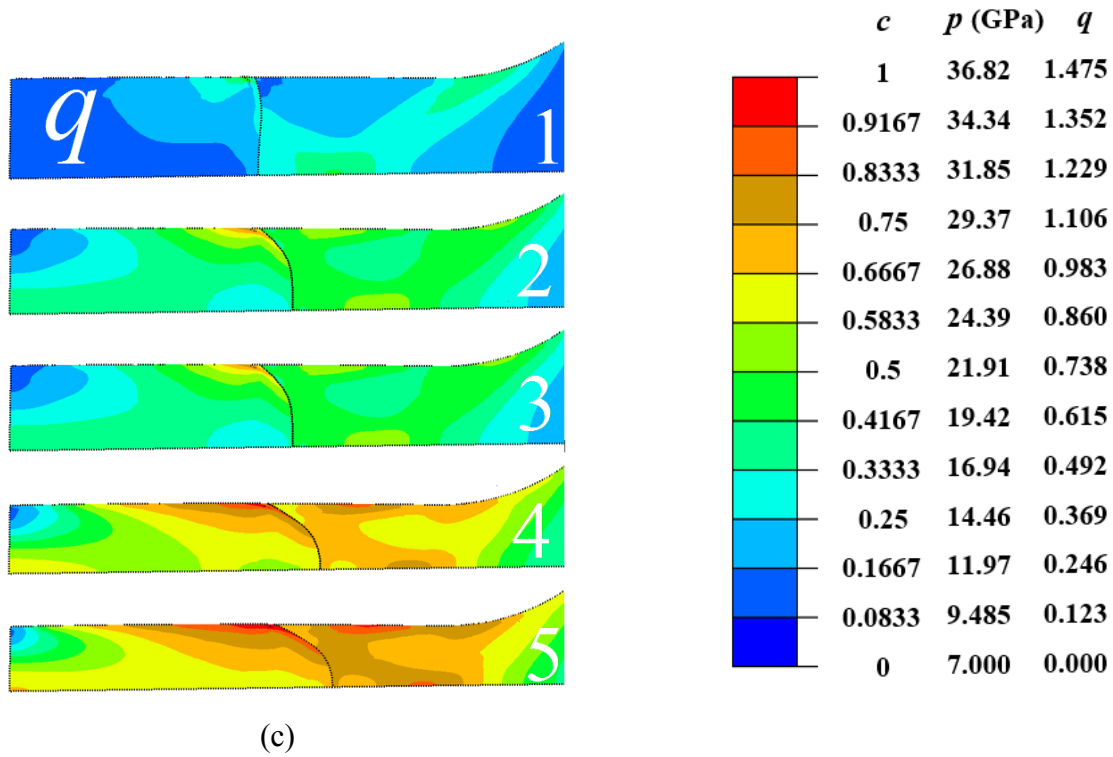
fraction in Fig. 2a is consistent with the pattern of the plastic strain distribution in Fig. 2c. Before torsion and during the rotation, Fig. 2b and Fig. 3 show that there are two regions for the pressure distribution in a gasket: the pressure gradient is small at a flat contact surface, but when the contact surface becomes inclined, the pressure dramatically decreases with a rising radial coordinate  $r$ . At the initial rotation from  $\varphi = 0$  to  $\varphi = 0.2$ , the pressure increases in the major central part of a sample but decreases at the periphery. This is caused by a thickness reduction and faster PT at the periphery. Specifically, it can be explained by a simplified equilibrium equation (see e.g. Feng and Levitas, 2017b; 2017d),

$$\frac{dp}{dr} = -\frac{2\tau_{rz}^c}{h}, \quad (21)$$

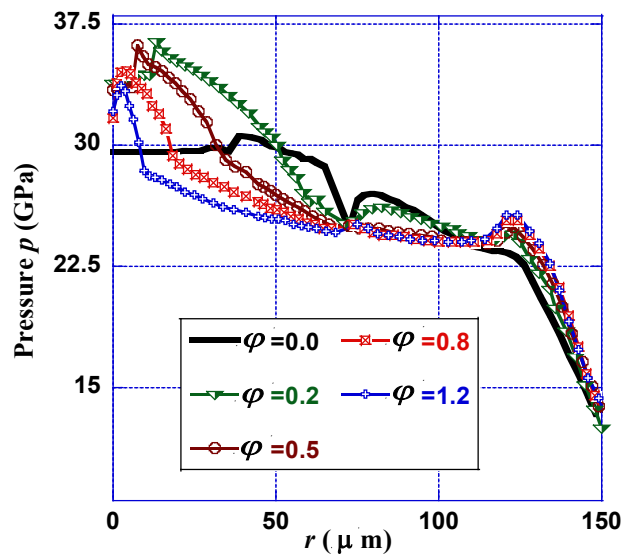
where  $h$  is the sample thickness and  $\tau_{rz}^c$  is the component of friction stress that is perpendicular to the circumferential direction. When the surface is flat,  $\tau_{rz}^c = \tau_{rz}$  is along the radial direction, but when the surface is inclined, it also has a component along the  $z$ -axis. During PT into a strong high-pressure phase wBN, hardening of the material can cause an increase in the shear stress  $\tau_{rz}^c$ . When the initial rotation rises from  $\varphi = 0$  to  $\varphi = 0.2$ , the fast PT process significantly increases the shear stress  $\tau_{rz} \approx \tau_{rz}^c$  as shown in Fig. 4 (a), and the thickness of the sample reduces as shown in Fig. 2 as well, which together provides a large pressure gradient based on Eq. (21) and, thus, pressure in the sample. At the same time, pressure reduces due to the volume decrease during PT, and this process prevails at the periphery of a sample. Increase in pressure during torsion is called the pressure self-multiplication effect, which was experimentally found in various materials (Blank and Estrin, 2014; Blank et al., 1984; Novikov et al., 1999), but without a gasket. With a gasket, the process of pressure redistribution at a constant compressive force is much more sophisticated. From  $\varphi = 0.2$  to  $\varphi = 1.2$ , the pressure in the sample decreases almost everywhere. There are three reasons for this: a significant reduction in the friction stress  $\tau_{rz}^c$  occurs at the major part of the

sample as shown in Fig. 4a, the large transformational volume reduction during PT reduces pressure in the sample, and the material flow from the center to the periphery causes an increase of the total contact area between the diamond, gasket, and sample at the constant force. Complex interaction between a heterogeneous increase in strength and a reduction in volume during PT leads to a complex pressure curve at the contact surface, with the maximum slightly away from the center. Very close to the center ( $r < 10 \mu\text{m}$ ), due to the small plastic strain shown in Fig. 2c, the PT rate is slow. Strong wBN surrounds weak hBN at the center, which causes reduction in pressure at the center. Due to high pressure, PT is completed in almost the entire sample at  $\varphi = 1.2$ ; therefore, a larger rotation is not considered.

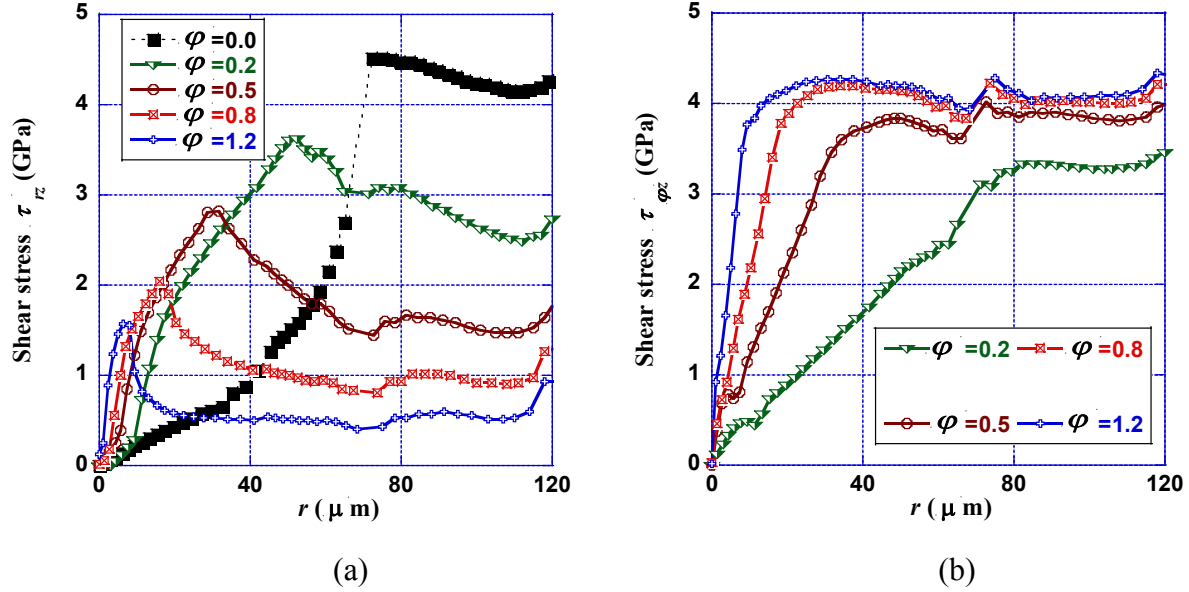




**FIG. 2.** Distributions of the volume fraction of high-pressure phase  $c$  (a), the pressure  $p$  in the sample and gasket ( $0 \leq r \leq 160 \mu\text{m}$ ) (b), and the accumulated plastic strain  $q$  (c) under a constant applied normal compressive stress  $\sigma_n = 0.64$  GPa. The rotation angle  $\varphi$  in radians is 0 (1), 0.2 (2), 0.5 (3), 0.8 (4), 1.2 (5).



**FIG. 3.** Distribution of pressure  $p$  at the contact surface of the sample and gasket under a fixed stress  $\sigma_n = 0.64$  GPa.



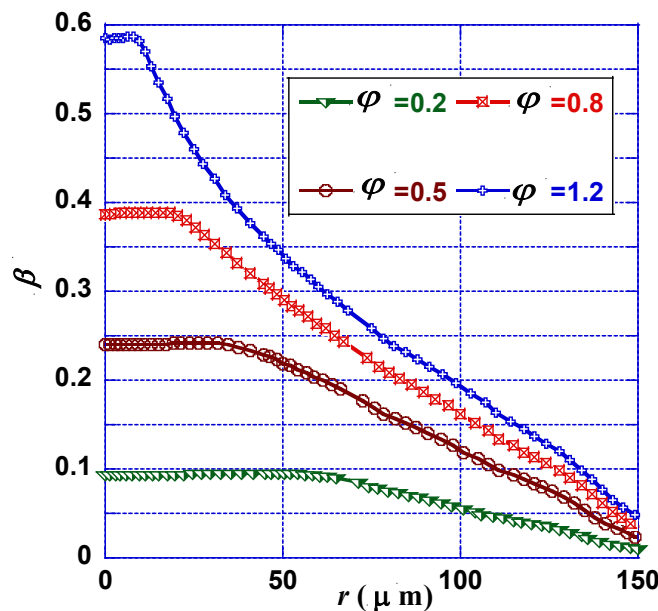
**FIG. 4.** Distributions of the shear stresses  $\tau_{rz}$  (a) and  $\tau_{\phi z}$  (b) at the contact surface of the sample and gasket in contact with the diamond anvil under a stress  $\sigma_n=0.64$  GPa.

Fig. 4 plots the evolutions of the shear stresses, radial  $\tau_{rz}$  and circumferential  $\tau_{\phi z}$ , at the contact surface of the sample and gasket. Before torsion, the circumferential shear stress is zero and  $\tau_{rz}$  continuously increases with a rising radial coordinate  $r$  in the sample, almost remaining constant at the gasket. At the center of the sample ( $r=0$ ), the shear stress is always zero due to symmetry as long as the surface is flat, and it grows, as usual, from the center to the periphery due to the increasing tendency of a sample to slide with respect to an anvil. In addition, this increase is enhanced due to growth in the volume fraction of wBN, and, consequently, the yield strength in shear along the radial direction. Before torsion, there is a jump in  $\tau_{rz}$  from the sample to the gasket, which is caused by a sudden change in material strength. Specifically, before torsion the sample is mostly hBN (see in Fig. 2a), which is a very soft material, but Re is a strong gasket. During torsion, however, material hardening due to PT in the sample occurs and the radial shear stress in a sample can surpass that in the gasket, as shown in Fig. 4a. During sliding in a gasket (Fig. 5), friction stress  $\tau_{rz}^c = \mu\sigma_c$  ( $\sigma_c$  is the normal contact stress), which is slightly below the yield strength in shear  $\tau_y = \sigma_y/\sqrt{3}$ . The contact stress  $\sigma_c$  in the gasket is close to the pressure  $p$  at the contact

surface, which does not vary significantly for the flat contact surface part ( $80 \mu\text{m} < r < 120 \mu\text{m}$ ); see Fig. 2b and Fig. 3. Therefore, the total friction shear stress does not change significantly before (see curve 1 in Fig. 4a) and during the torsion. With a rising rotation angle, the circumferential contact stress  $\tau_{\varphi z}$  in the gasket continuously rises, which causes a reduction of the radial friction stress  $\tau_{rz}$  to keep the sliding condition satisfied:

$$\sqrt{\tau_{rz} + \tau_{\varphi z}} \approx \tau_{rz}^c = \mu\sigma_c. \quad (22)$$

where “ $\approx$ ” is changed to “=” if the contact surface is completely flat. Here we have a slight bending at the contact surface of gasket surface, as shown in Fig. 6, so “ $\approx$ ” is used in Eq. (22). For the sample, the circumferential shear stress rises with an increase of the rotational angle, similar to that in the gasket. The radial shear stress  $\tau_{rz}$  in a sample in the region close to the center increases during the entire torsion in Fig. 4a, which is caused by material hardening with a continuous increase in the wBN volume fraction. From compression to a rotation with  $\varphi = 0.2$ , the radial shear stress increases significantly in the entire sample. At the contact surface near the sample-gasket boundary, the volume fraction of wBN is close to 1 at  $\varphi = 0.2$ , and further increasing of the rotation angle  $\varphi$  then leads to the reduction of the stress  $\tau_{rz}$ , which is caused by an increasing circumferential stress  $\tau_{\varphi z}$ .



**FIG. 5.** Distribution of the rotation angle  $\beta$  of the material points of the gasket and sample at the surface in contact with diamond, with respect to the symmetry plane ( $z=0$  plane) under a stress  $\sigma_n=0.64$  GPa.

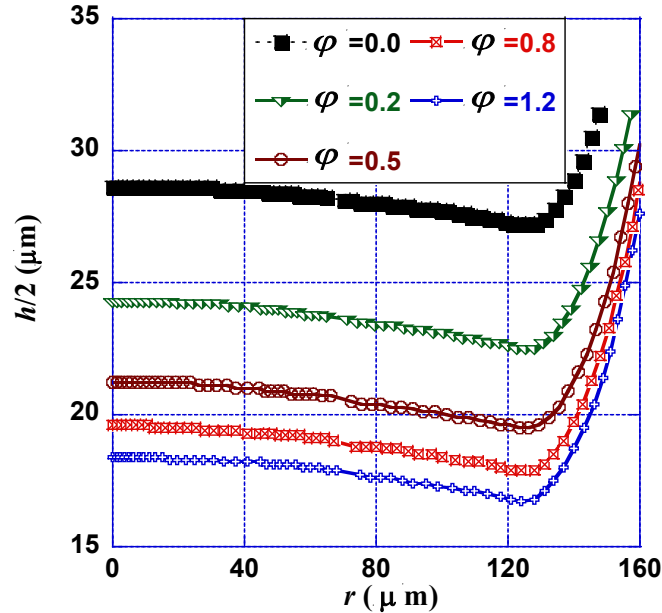


**FIG. 6.** A half of the thickness of the sample and gasket  $h/2$  (or the  $z$  coordinate at the contact surface of diamond) under  $\sigma_n=0.64$  GPa.

Fig. 5 presents the rotation angle  $\beta$  of the material points at the surface of the sample and gasket in contact with the diamond, with respect to the symmetry plane ( $z=0$ ). The horizontal line for  $\beta$  in Fig. 5 corresponds to the cohesion region between the sample and the diamond, where  $\beta$  is close to  $0.5\varphi$  (see below), while the nonzero slope indicates sliding at the contact surface. With a rotation angle  $\varphi = 0.2$ , the sliding exists in the entire contact surface between the diamond and the gasket, and it initiates at the very periphery of a contact surface between the diamond and the sample. With an increase of the rotation angle, the cohesion zone between the diamond and the sample reduces, and at  $\varphi = 1.2$ , the cohesion zone is only localized at very center of the contact area for  $r < 9 \mu\text{m}$ . In the cohesion zone,  $\beta$  corresponds to the rotation angle of the contact diamond surface with respect to the symmetry plane, and if the diamond is rigid the relation between  $\beta$  and  $\varphi$  is  $\beta = \varphi/2$ . Consequently,  $\varphi/2 - \beta$  for the cohesion zone represents the relative elastic twisting angle between the top and bottom contact surface of the upper anvil.

Initially,  $\varphi/2 - \beta$  is almost zero, and with a rising rotation angle, the magnitude gradually increases to about 0.015 for  $\varphi = 1.2$ . Sliding of the material with respect to the anvil in RDAC was observed experimentally, even above 100 GPa (Nomura et al., 2017).

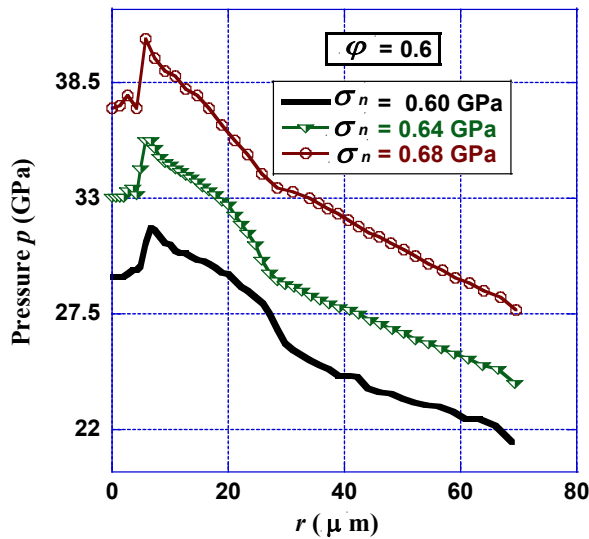
Fig. 6 exhibits a half of the thickness of the sample and gasket  $h/2$ , which also represents the  $z$  coordinate at the contact surface of the diamond anvil. In the undeformed state,  $h/2$  is  $40 \mu\text{m}$  and reduces to  $28 \mu\text{m}$  at  $\sigma_n = 0.64 \text{ GPa}$  and  $\varphi = 0$ . The  $12 \mu\text{m}$  thickness reduction only causes a very slight PT. From  $\varphi = 0$  to  $\varphi = 1.2$  under a fixed  $\sigma_n$ , the thickness reduction is  $11 \mu\text{m}$  and the wBN volume fraction increases almost from 0 to 1 throughout the entire sample. Such a fast PT during rotation occurs due to two reasons. First, for compression the plastic flow is mostly from the thickness reduction, and for torsion there is a significant plastic flow along both the thickness and circumferential directions. Second, high pressure intensifies a PT, and during compression pressure varies from zero to around 30 GPa. For rotation, the pressure in the sample is high during the entire process and is even higher than 30 GPa in the central region (see Fig. 3). In the undeformed state, the slope of  $h/2$  is zero, but with compression to  $\sigma_n = 0.64 \text{ GPa}$  and  $\varphi = 0$ , cupping of the diamond anvil appears (i.e. the negative slope). With a rising rotation angle, the cupping of diamond becomes more severe. Specifically,  $h/2|_{r=0} - h/2|_{\min}$  is only  $1.4 \mu\text{m}$  before torsion, and it increases to  $1.7 \mu\text{m}$  at  $\varphi = 1.2$ , where  $h/2|_{r=0}$  is the  $z$  coordinate of the diamond contact surface at  $r=0$  and  $h/2|_{\min}$  is the minimum of the  $z$  coordinate of the diamond contact surface.

#### 4.2 Effect of the applied compressive stress $\sigma_n$

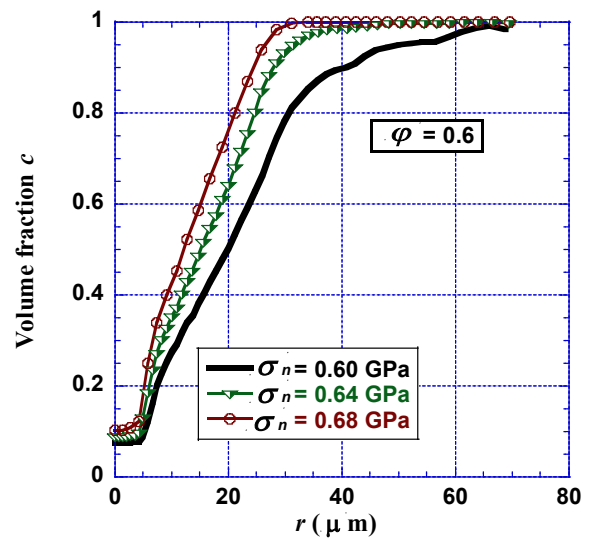
In Sec. 4.1, the applied stress is chosen as  $\sigma_n = 0.64 \text{ GPa}$ . Here, the effect of  $\sigma_n$  is discussed during rotation by taking three  $\sigma_n$  as 0.6, 0.64, and 0.68 GPa for three simulations, respectively. Fig. 7 plots the distribution of pressure  $p$ , the volume fraction  $c$  of wBN, and the accumulated plastic strain  $q$  at the rotation angle 0.6, under three different  $\sigma_n$ . With the same rotation angle, the slight increase in  $\sigma_n$  causes a significant rise in pressure at the contact surface (Fig. 7a). This is because of a large ratio of the areas of the top surface (see  $AB$  in Fig. 1b) and the flat surface of an anvil ( $CK$  in Fig. 1c):  $(1.05/0.15)^2 = 49$ . If we include an inclined contact surface

between the diamond and the sample ( $KG$  in Fig. 1c) and consider the horizontal area with a radius corresponding to point  $G$  (Fig. 1c), the ratio is  $(1.05/(0.15+0.04))^2 = 30.54$ . Thus, for  $\sigma_n = 0.6$  GPa, the averaged stresses over these two bottom areas are 29.4 GPa and 18.32 GPa, respectively.

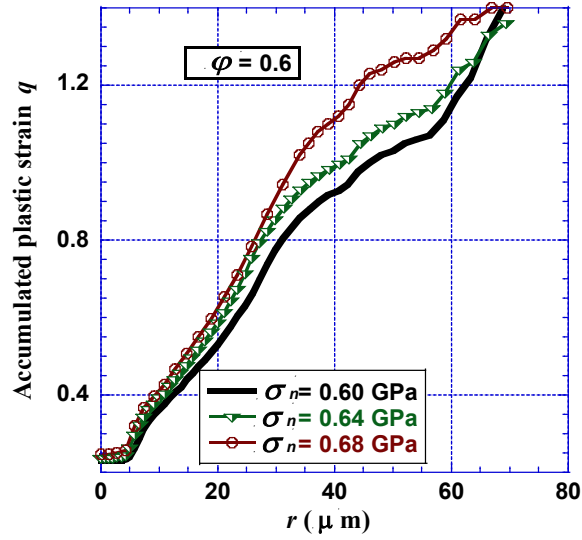
With the increase of compressive stress  $\sigma_n$  from 0.6 to 0.64 and to 0.68 GPa, the maximum pressure at the sample increases from 31.6 to 35.8 and to 40.6 GPa, respectively. A higher pressure in the sample intensifies the PT, and thus the wBN volume fraction is larger in Fig. 7b if the applied stress  $\sigma_n$  is higher. For  $r > 30 \mu\text{m}$ , the PT is completed for  $\sigma_n = 0.64$  and 0.68 GPa, and hBN almost completely transforms into wBN for  $\sigma_n = 0.6$  GPa. Due to an increase in the normal contact stress  $\sigma_c$  at the sample and the gasket surfaces making contact with the diamond anvil, the Coulomb friction  $\mu\sigma_c$  increases, contact sliding reduces, and the circumferential plastic flow intensifies. In addition, the sample thickness decreases, causing an additional material radial plastic flow. Fig. 7c confirms that, with a larger compressive stress, the plastic strain is larger at the contact surface. However, at the very periphery the plastic strain for  $\sigma_n = 0.60$  GPa slightly surpasses that for  $\sigma_n = 0.64$  GPa, which is slightly off this tendency. This is due to the high volume fraction of harder wBN, which is more difficult to plastically deform. Large plastic strain and high pressure both intensify the PT progress, and the pressure effect surpasses the effect of plastic strain at the very periphery of the sample between the cases of  $\sigma_n = 0.60$  and 0.64 GPa.



(a)

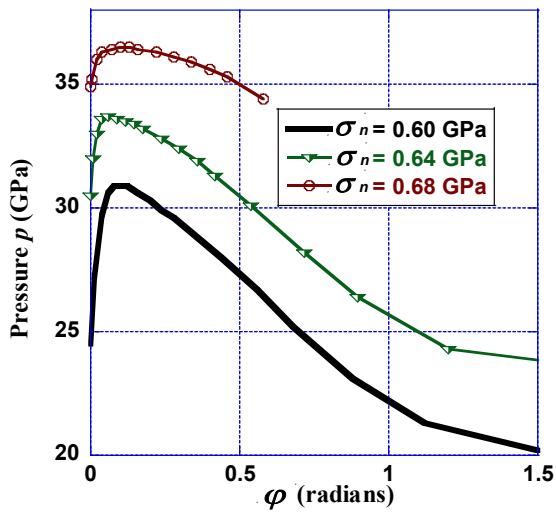


(b)

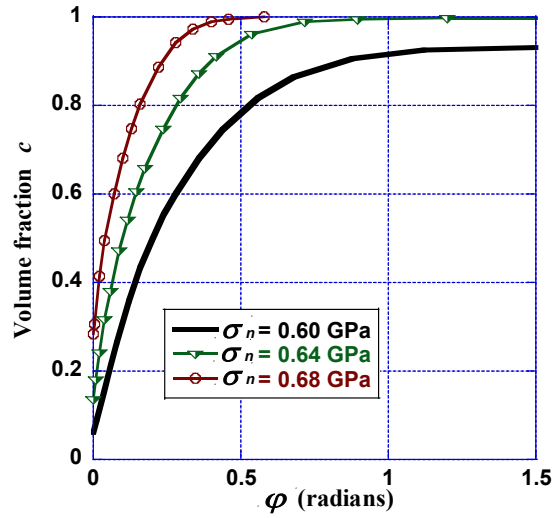


(c)

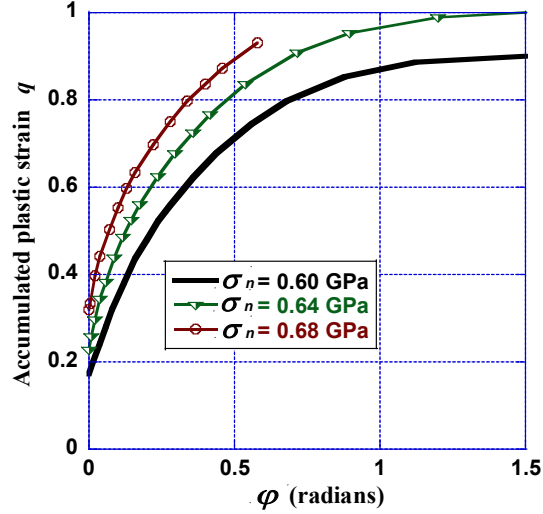
**FIG. 7.** Distributions of the pressure  $p$  (a), volume fraction of the high-pressure phase  $c$  (b), and accumulated plastic strain  $q$  (c) at the contact surface of the sample at the rotation angle  $\varphi = 0.6$  radians under various applied stresses  $\sigma_n$ .



(a)



(b)



(c)

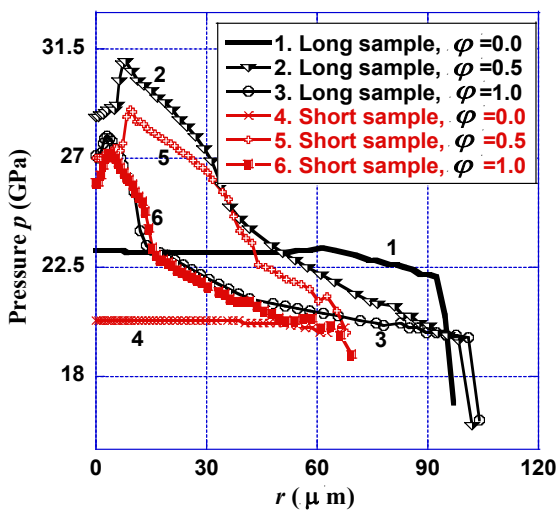
**FIG. 8.** The variations of the pressure  $p$  (a), the wBN volume fraction  $c$  (b), and the accumulated plastic strain  $q$  (c) at the center of the sample  $F$  vs. the rotation angle  $\phi$  under various applied stresses  $\sigma_n$ .

Fig. 8 shows that the increasing stress  $\sigma_n$  raises the pressure curves  $p$  vs.  $\phi$ ,  $c$  vs.  $\phi$ , and  $q$  vs.  $\phi$ . Reduction in the transformation rate with increasing rotation is explained by increasing contact sliding and reduction in the rate of plastic straining (Fig. 8c). The contact sliding increases with reducing  $\sigma_n$ ; this is why, for  $\sigma_n = 0.6$  GPa, the rate of plastic strain and transformations is very low  $\phi$ . This is the reason why, with a strong Re gasket, to obtain a fully transformed sample, we apply a very large compressive stress to obtain a pressure  $p$  that much higher than  $p_\varepsilon^d$ .

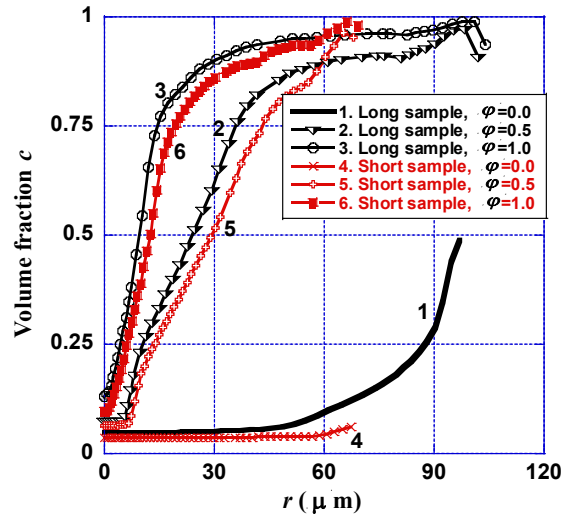
### 4.3 Effect of the sample radius

The total radius of a sample plus gasket is fixed as  $150 \mu\text{m}$ . Consequently, a longer sample means a shorter gasket and vice versa. Results for the sample radius of  $70$  and  $100 \mu\text{m}$  are presented in Fig. 9. The Re gasket is much stronger than hBN but much weaker than wBN. Fig. 9 shows that, before torsion, the pressure  $p$  in the longer sample is larger than in the shorter sample, and the pressure in the sample is homogeneous for both cases, excluding the periphery of a sample. With the shorter gasket, the material's radial flow is intensified under the same compressive force, leading to a thinner sample. Based on Eq. (22), a smaller thickness leads to a larger pressure

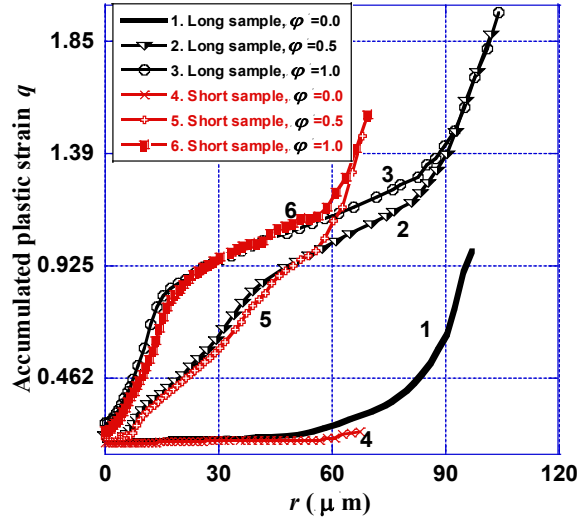
gradient and thus higher pressure in the gasket and, consequently, in the sample. A faster plastic straining and higher pressure cause a faster PT rate (Fig. 9b). Consequently, before torsion, the pressure, the volume fraction of high-pressure phase, and the accumulated plastic strain are much higher in the longer sample. However, a fast PT in a longer sample causes fast material hardening, which slows down plastic deformation and the thickness reduction and reduces the PT rate. Therefore, with an increasing rotation angle, due to material hardening during PT the differences between these two sample in the pressure, the volume fraction, and the plastic strain reduce. For  $\varphi=1.0$ , the pressure, volume fraction, and plastic strain are almost the same except at a very small region at the periphery. One may conclude that, with a strong gasket, a moderate increase of the sample radius does not reduce and may even slightly increase the PT rate, and a fully transformed sample can be achieved with a large rotation angle. Consequently, one can obtain a large volume of the high-pressure phase. However, for a weak gasket or no gasket, because hBN is a very soft material, a low pressure can be achieved only under compression and torsion, and a fully transformed sample or a large transformed volume is impossible; see the result for the zirconium sample in RDAC (Feng et al., 2018b).



(a)



(b)



(c)

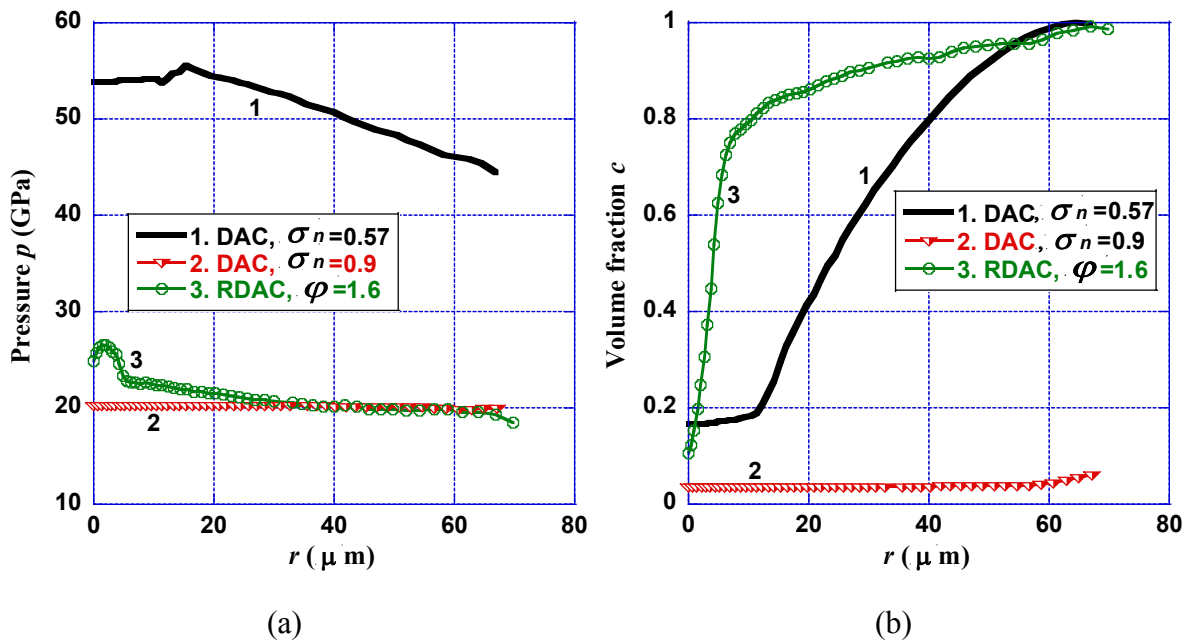
**FIG. 9.** The variations of the pressure  $p$  (a), the wBN volume fraction  $c$  (b), and the accumulated plastic strain  $q$  (c) under an applied stress  $\sigma_n = 0.57$  GPa for the short and long samples and different rotation angles.

#### 4.4 Comparison between DAC and RDAC

A DAC and a RDAC have the same axisymmetric geometry and geometric parameters. However, torsion in RDAC transforms a 2D problem for compression in DAC into a 3D problem. Fig. 10 shows the difference between the distributions of the pressure, wBN volume fraction, and accumulated plastic strain at the contact surface in DAC and RDAC. Curves 1 and 2 in Fig. 10 are for compression in DAC with the applied stresses  $\sigma_n = 0.9$  and  $0.57$  GPa, respectively, and curve 3 is for torsion with the rotation angle  $\varphi = 1.6$  and under  $\sigma_n = 0.57$  GPa. Without torsion under  $\sigma_n = 0.57$  GPa, the pressure is very homogeneous, and plastic strain and the wBN volume fraction are homogeneous as well (with a small exception at the periphery) and small. Torsion under the same force produces an intense plastic flow and reduces the thickness of a sample, resulting in the pressure gradient in a sample and a corresponding increase in pressure at the sample center. Large plastic flow causes an intense PT throughout the entire sample, excluding the central part.

For DAC, the only way to generate plastic straining is to increase the applied stress  $\sigma_n$ ; it thus leads to a very high pressure in the sample (see curves 1 and 2). Because the pressure is already higher than the minimum pressure for strain-induced PT  $p_\varepsilon^d$ , such a pressure increase is unnecessary and unwanted, but there is no other way. The pressure in curve 1 is much higher and

more heterogeneous, but the plastic strain and wBN volume fraction in curve 1 are still much smaller than for RDAC in curve 2. For a representative point such as the center of a sample, the pressure  $p$  versus the volume fraction of the high-pressure phase  $c$  is plotted for DAC and RDAC at  $\sigma_n = 0.57$  GPa in Fig. 10d. The volume fraction  $c$  is an increasing function of the pressure  $p$  in DAC. However, with  $c$  varying from 0.1 to 0.8, the pressure changes much more moderately in RDAC, it increases at the beginning, and then decreases. To achieve the same amount of high-pressure phase as in DAC, the required pressure is much lower in RDAC (as shown in Fig. 10d), which reduces the difficulties to create the high-pressure environment and increases the anvils' service lifetime. In addition, the high-pressure phase with a large volume fraction is obtained as shown in RDAC in Fig. 10b, and the pressure is still relatively homogeneous. A homogeneous pressure in the sample in RDAC is beneficial to extract the material parameters for strain-induced PTs (our paper with a gasket). With proper optimization of the geometric parameters and properties of a gasket, the pressure in a sample can be reduced closer to  $p_\varepsilon^d$ , as we demonstrated in (our paper with a gasket) for a simplified generic model (Feng and Levitas, 2016).



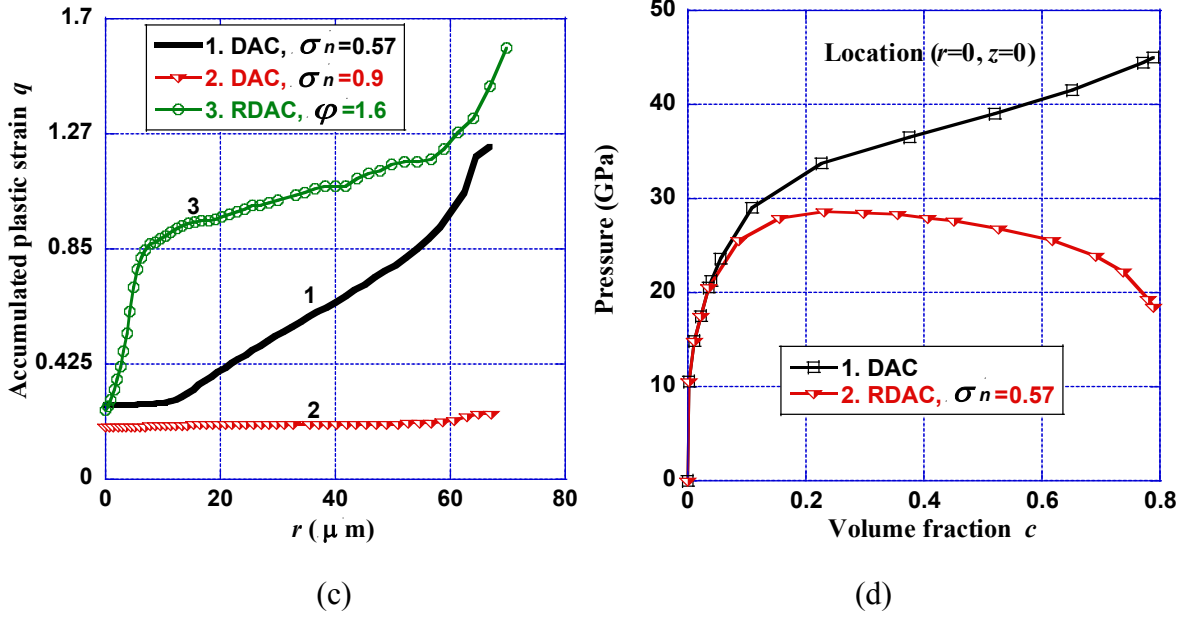


**FIG. 10.** The variations of the pressure  $p$  (a), the volume fraction of the high-pressure phase  $c$  (b), and the accumulated plastic strain  $q$  (c) at the contact surface. Curves 1 and 2 are results for DAC under the applied  $\sigma_n=0.57$  and  $0.9$  GPa, respectively, and curve 3 stands for RDAC under  $\sigma_n=0.57$  GPa and  $\varphi=1.6$ . (d) The pressure vs. the volume fraction of wBN  $c$  at the center of sample in DAC and RDAC at  $\sigma_n=0.57$  GPa.

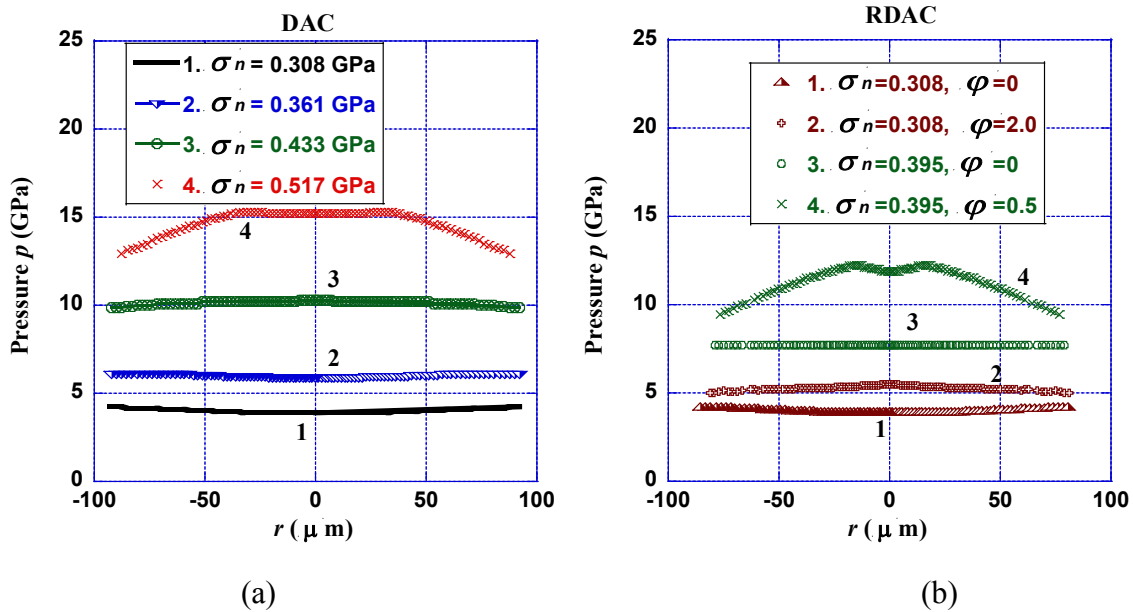
#### 4.5 Quasi-Homogeneous Pressure in DAC and RDAC

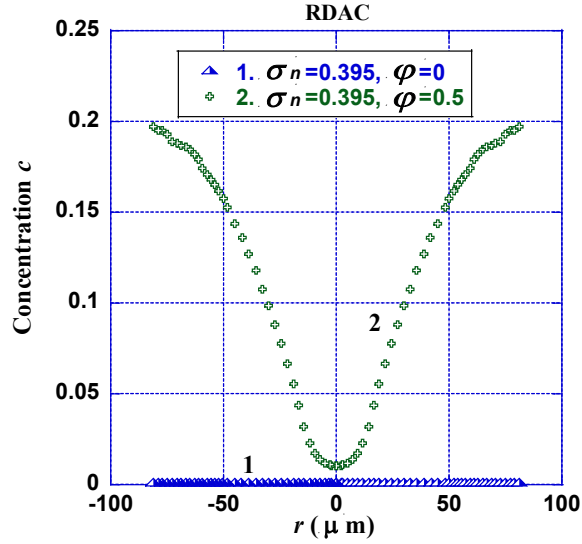
Levitas et al. (2006) experimentally studied the strain-induced PT from hBN to wBN on a hBN sample with a radius of  $100\ \mu\text{m}$  in a gasket made of stainless steel. A quasi-homogeneous pressure at the contact surface was obtained in DAC at compression up to  $10$  GPa and in RDAC when the pressure was below  $12$  GPa. Here, we will model this experiment.

Because the pressure below  $16$  GPa in the simulation of this section and the steel gasket is a strong material, there is no need to consider high-order elastic constants for the gasket. The material properties for the gasket used in the simulation are from (Levitas et al., 1996): the shear modulus  $G=104$  GPa and the Lamé coefficient  $\lambda_g=106$  GPa, the yield strength at the zero pressure  $\sigma_0=2$  GPa and the coefficient for the pressure effect on the yield strength  $b=0.002$ . The sample material is the same as that which is mentioned in Sec. 2. The sample radius and the culet radius are  $100$  and  $250\ \mu\text{m}$ , as in experiment (Levitas et al., 2006). When the pressure in

DAC is below 10 GPa, it is very homogeneous throughout the entire contact surface (Fig. 11a), consistent with the experiment in Levitas et al. 2006. The heterogeneity increases for pressures around 15 GPa, but the pressure still does not vary significantly in the sample. For RDAC (Fig. 10b), we find that, with or without torsion, in curve 1 and 2 under  $\sigma_n=0.308$ , the pressure is very homogeneous and does not change significantly after torsion. This is also observed in experiment without PT (Levitas et al. 2006). From curve 3 to curve 4 ( $\sigma_n=0.395$  GPa), a PT takes place (Fig. 11c) and pressure increases during torsion; the pressure distribution recollects what was observed in experiment (Levitas et al. 2006), but is slightly more heterogeneous. These results create an opportunity to optimize gasket properties and geometry to achieve the homogeneous pressure in both DAC and RDAC. Homogenous pressure is also important to avoid misinterpretation of PT pressure due to radial flow. Indeed, with a large pressure gradient, PT may occur at relatively high pressure but the high-pressure phase may be convectively moved to the low-pressure region, where it will be found.

In DAC for  $\sigma_n=0.395$  GPa, the volume fraction of the high-pressure phase is almost zero in both the simulation and the experiment (see curve 1 in Fig. 11c). For  $\varphi=0.5$ , however, we can achieve the obvious PT (Fig. 11c). Note that plastic strain is non-uniform along the radius, which results in heterogeneity of the volume fraction of wBN.





(c)

**FIG. 11.** The variation of the pressure  $p$  (a and b) and the wBN volume fraction  $c$  (c) at the contact surface. In (a) for DAC, the applied stresses are  $\sigma_n=0.308$  (1), 0.361 (2), 0.443 (3) and 0.517 (4) in GPa. In (b) for RDAC, the stresses are  $\sigma_n=0.308$  (1, 2), 0.395 (3, 4) in GPa and the rotation angle  $\varphi=0$  (1, 3) 2.0 (2), and 0.5 (4) in radians. In (c) for RDAC, the stress is  $\sigma_n=0.395$  GPa and  $\varphi=0$  (1) and 0.5 (2).

## 5. Concluding remarks

In this paper, the first modeling results for three-dimensional coupled plastic flow and strain-induced PT from hBN to wBN within the strong Re gasket under high-pressure torsion in a RDAC are obtained. The theory includes finite elastic, transformational, and plastic deformations, the nonlinear Murnaghan elasticity rule, and pressure-dependent yield strength for both BN phases and an Re gasket, as well as strain-controlled and pressure-dependent kinetics for hBN to wBN PT. A diamond anvil is described by the third-order and finite strain elasticity for cubic crystals. FEM and code ABAQUS with the developed UMAT subroutine are utilized for solution of the boundary-value problems, including the contact problem at the boundary between the diamond, the sample, and the gasket.

Quantitative information is obtained on the evolutions of the stress tensor, the accumulated plastic strain, the volume fraction of wBN phase throughout the entire sample, and slip-cohesion transitions during torsion under a fixed compressive load in RDAC. Complex evolution of all fields is caused by a large difference in the strength and elastic moduli of wBN and hBN (by 30 and 10-20 times, respectively), which causes transformational strengthening during PT and pressure growth. On the other hand, the large volumetric transformation strain of 0.3 significantly reduces pressure. Strength of a gasket is between that for hBN and wBN, and stresses redistribute between the gasket and the sample during torsion and PT. All of this results in the change from quasi-homogeneous pressure at the contact surface of a sample after compression to non-monotonous and non-monotonously evolving pressure curves during torsion. In particular, pressure growth in the sample under a constant compressive force is predicted; this is called the pressure self-multiplication effect, and it was observed experimentally in a number of materials (Blank and Estrin, 2014; Blank et al., 1984; Novikov et al., 1999) but loaded without a gasket. One more contribution to this complexity comes from the redistribution of radial  $\tau_{rz}$  and circumferential  $\tau_{\varphi z}$  contact shear (friction) stresses. The latter grows monotonously during torsion. Radial stress  $\tau_{rz}$  increases at the region near the center of a sample due to transformational hardening during PT, and  $\tau_{rz}$  initially increases at the periphery for the same reason and then reduces.

Contact sliding of the sample and the gasket with respect to the anvil, especially in circumferential directions, plays a crucial role in determining actual plastic deformation and, consequently, the volume fraction of wBN. With a small rotation angle of 0.2, the sliding initiates at the very periphery of a sample, i.e. the sample is practically subjected to the same torsion as prescribed by an anvil. With an increase of the rotation angle, the cohesion zone between the diamond and the sample reduces, and at  $\varphi=1.2$ , the cohesion zone is only located at the very center of a sample. This means that the torsion angle at the periphery of a sample is twice as small as the torsion prescribed by an anvil, which was never analyzed experimentally.

All of these processes lead to a complex heterogeneous evolution of the volume fraction of wBN. After compression, PT begins while pressure is far above the minimum pressure for strain-induced PT,  $p_e^d$ . During torsion, the wBN propagates from corner D (where the sample, gasket, and anvil meet) and center F toward each other, with the major part of the sample completely

transformed at  $\varphi = 1.2$  except for the very small region near the contact surface at the center of the sample. PT evolution patterns are mostly governed by plastic strain rather than pressure. Despite the modest maximum pressure below 37 GPa, the diamond anvil deformation at the center becomes obvious, which affects the processes in a sample.

The increase in the compressive stress  $\sigma_n$  for RDAC increases the plastic strain, pressure, and PT rate. Surprisingly, the increase in the sample radius essentially increases the pressure and extension of PT under compression. However, the effect of the sample radius is reduced with a rising rotation angle. Consequently, one can use a larger sample to obtain a larger amount of the high-pressure phase, and optimization of the sample radius is possible. However, this is based on the prerequisite that a strong gasket material such as Re is used.

Comparison between processes in DAC and RDAC shows that, to achieve the same amount of high pressure in RDAC, the required pressure can be much lower than that in DAC. This reduces the required force and requirements to the device, which produces this force (e.g. to press for a large scale high-pressure torsion) and increases the anvils' service lifetime. An important point is that, by optimizing the geometric parameters and properties of a gasket, one can run and complete the PT at a pressure near the minimum pressure for strain-induced PT,  $p_\varepsilon^d$ . This is impossible for DAC, where the only way to increase plastic strain is to increase force and pressure.

In addition, the high-pressure phase with a high volume fraction can be obtained under a quasi-homogenous pressure in RDAC due to the relatively low pressure. This is not the case for DAC, where large compression and accompanying high pressure are required to reach almost complete PT. A homogeneous pressure in the sample in RDAC is beneficial for extracting the material parameters for strain-induced PTs. Also, in our simulation, we reproduced the experimental results from Levitas et al. 2006 on the quasi-homogeneous pressure in DAC and RDAC before and during PT.

The simulation results provide an important insight into coupled PTs and plastic flow in a material under high pressure and large plastic shear in RDAC. They can be used for optimum design of experiments and extraction of material parameters during PTs, as well as optimization and control of PTs by variation of the geometry in RDAC, loading conditions, and gasket material.

While this paper is focused on coupled plasticity and PT under high pressure at static loadings, similar processes under dynamical loadings are also very important and are an ongoing and promising research area. Thus, coupling between plasticity and PT for single and polycrystalline iron or iron-based materials under shock compression was studied by molecular dynamical simulations in Wang et al., 2014, 2015, 2017. Shock-induced plasticity and structural PTs in ceramic materials such as AlN (Branicio, et al. 2013) and SiC (Li, et al. 2017) were also investigated by molecular dynamic simulations. A model for the time-dependent plastic response of a material to dynamic loading is developed in (Colvin et al., 2009) and the model is applicable to the simulation of experimental velocity interferometry, in which iron is shocked to pressures beyond the  $\alpha$  to  $\epsilon$  PT pressure. A high-rate, single-crystal model for cyclotrimethylene trinitramine, including PT and plastic slip, is proposed in (Addessio et al., 2017). The two-phase equilibrium and phase diagram for an elastic-plastic deformed system under non-hydrostatic stress conditions is formulated in (Zhang et al., 2018), and the formalism is employed to quantitatively interpret the scatter in the transition pressure of the  $\alpha - \omega$  transformation in titanium observed in experiments. Feng et al. (2018a) proposed a thermodynamically-consistent system of equations for coupled elasticity, plastic slip and twinning for high-purity single crystal titanium in the framework of large deformation, and used FEM to investigate the titanium sample loaded by a split-Hopkinson pressure bar. However, PTs were not treated as strain-induced in the papers cited above. Exploring potential plastic strain-induced mechanism and kinetics for dynamic PTs may be a promising direction in these studies.

## **Acknowledgements**

The support of ARO (W911NF-17-1-0225), NSF (DMR-1434613), ONR (N00014-16-1-2079), and Iowa State University (Vance Coffman Faculty Chair Professorship) is gratefully acknowledged.

## **References**

- Addessio, F.L., Luscher, D.J., Cawkwell, M.J., Ramos, K.J., 2017. A single-crystal model for the high-strain rate deformation of cyclotrimethylene trinitramine including phase transformations and plastic slip. *J. Appl. Phys.* 121, 185902.
- Alexandrova, M. M., Blank, V. D., and Buga, S. G., 1993. Phase-Transitions in Ge and Si under Shear-Stress at Pressures up to 12 Gpa and P-T-Gamma Diagrams of These Elements. *Solid State Phys.* 35, 1308-1317.
- Bassett, W. A., 2009. Diamond anvil cell, 50th birthday, *High Pressure Res.* 29, 163-186.
- Blank, V.D., Boguslavsky, Y.Y., Eremets, M.I., Itskevich, E.S., Konyaev, Y.S., Shirokov, A.M., Estrin, E.I., 1984. Pressure Self-Multiplication Effect on Phase-Transition under Quasi-Hydrostatic Conditions. *Zh. Eksp. Teor. Fiz.* 87, 922-926.
- Blank V. D., Dubitsky, G. A. 1995. High pressure science and technology in Proceedings of Joint XV AIRAPT and XXXIII EHPRG International Conference, Warsaw, edited by W. A. Trzeciakowski (World Scientific Publishing, London), pp. 325–327.
- Blank, V. D., Estrin, E. I., 2014. *Phase Transitions in Solids under High Pressure*, CRC Press, New York.
- Blank, V. D., Malyushitska, Z. H., and Kulnitskiy, B. A., 1993. Structural mechanisms of Si (Ge) I to III phase transformations. *High Press. Phys. Eng.* 3, 28.
- Branicio, P. S., Nakano, A., Kalia, R. K., Vashishta, P., 2013. Shock loading on AlN ceramics: A large scale molecular dynamics study. *Int. J. Plast.* 51, 122-131.
- Bridgman, P.W., 1935. Effects of high shearing stress combined with high hydrostatic pressure. *Phys. Rev.* 48, 825-847.
- Britun, V.F., Kurdyumov, A.V., 2000. Mechanisms of martensitic transformations in boron nitride and conditions of their development. *High Press. Res.* 17, 101-111.
- Clayton, J.D., 2011. *Nonlinear Mechanics of Crystals*. Springer, New York.
- Colvin, J. D., Minich R. W., Kalantar D. H., 2009. A model for plasticity kinetics and its role in simulating the dynamic behavior of Fe at high strain rates. *Int. J. Plast.* 25, 603-611.
- Dias, R. P., Silvera, I. F., 2017, Observation of the Wigner-Huntington transition to metallic hydrogen, *Science* 355, 715–718.
- Dubrovinsky, L., Dubrovinskaia, N., Bykova, E., Bykov, M., Prakapenka, V., Prescher, C., Glazyrin, K., Liermann, H. P., Hanfland, M., Ekholm, M., Feng, Q., Pourovskii, L. V., Katsnelson, M. I., Wills, J. M., and Abrikosov, I. A., 2015. The most incompressible metal osmium at static pressures above 750 gigapascals. *Nature* 525, 226-229.
- Dubrovinsky, L., Dubrovinskaia, N., Prakapenka, V. B., and Abakumov, A. M., 2012. Implementation of micro-ball nanodiamond anvils for high-pressure studies above 6 Mbar. *Nat. Commun.* 3, 1163.
- Edalati, K., Daio, T., Arita, M., Lee, S., Horita, Z., Togo, A., Tanaka. I., 2014. High-pressure torsion of titanium at cryogenic and room temperatures: Grain size effect on allotropic phase transformations. *Acta Mater.* 68, 207-213.
- Edalati, K., Horita, Z., 2016. A review on high-pressure torsion (HPT) from 1935 to 1988. *Mat. Sci. Eng. A.* 652, 325-352.
- Edalati, K., Horita, Z., Yagi, S., Matsubara, E., 2009. Allotropic phase transformation of pure zirconium by high-pressure torsion. *Mater. Sci. Eng. A* 523, 277-281.
- Feng, B., Bronkhorst, Addessio, F.L., Morrow, B.M., Cerreta, E.K., Lookman, T. Lebensohn, R.A., and Low T., 2018a. Coupled elasticity, plastic slip, and twinning in single crystal titanium loaded by split-Hopkinson pressure bar. *J. Mech. Phys. Solids* 119, 274-297.

- Feng, B., Bronkhorst, Addessio, F.L., Morrow, E.K., W.H. Li, Lookman, B.M., Cerreta, 2018c. Coupled nonlinear elasticity, plastic slip, twinning, and phase transformation in single crystal titanium for plate impact loading. (Submitted)
- Feng, B., and Levitas, V. I., 2016. Effects of gasket on coupled plastic flow and strain-induced phase transformations under high pressure and large torsion in a rotational diamond anvil cell. *J. Appl. Phys.* 119, 015902.
- Feng, B., and Levitas, V. I., 2017a. Coupled elastoplasticity and plastic strain-induced phase transformation under high pressure and large strains: formulation and application to BN sample compressed in a diamond anvil cell. *Int. J. Plast.* 96, 156-181.
- Feng, B., and Levitas, V. I., 2017b. Large Elastoplastic Deformation of a Sample under Compression and Torsion in a Rotational Diamond Anvil Cell under Megabar Pressures. *Int. J. Plast.* 92, 79-95.
- Feng, B., and Levitas, V. I., 2017c. Plastic flows and strain-induced alpha to omega phase transformation in zirconium during compression in a diamond anvil cell: Finite element simulations. *Mat. Sci. Eng. A-Struct.* 680, 130-140.
- Feng, B., and Levitas, V. I., 2017d. Pressure self-focusing effect and novel methods for increasing the maximum pressure in traditional and rotational diamond anvil cells. *Sci. Rep.* 7, 45461.
- Feng, B., Levitas, V. I., and Hemley, R. J., 2016. Large elastoplasticity under static megabar pressures: formulation and application to compression of samples in diamond anvil cells. *Int. J. Plast.* 84, 33-57.
- Feng, B., Levitas, V. I., and Ma, Y. Z., 2014a. Strain-induced phase transformation under compression in a diamond anvil cell: Simulations of a sample and gasket. *J. Appl. Phys.* 115, 163509.
- Feng, B., Levitas, V. I., and Kamrani, M. 2018b. Coupled strain-induced alpha to omega phase transformation and plastic flow in zirconium under high pressure torsion in a rotational diamond anvil cell. *Mat. Sci. Eng. A-Struct.* 731, 623-633.
- Feng, B., Zarechnyy, O. M., and Levitas, V. I., 2013a. Strain-induced phase transformations under compression, unloading, and reloading in a diamond anvil cell. *J. Appl. Phys.* 113, 173514. Feng, B., Zarechnyy, O. M., and Levitas, V. I., 2014b. Strain-induced phase transformations under high pressure and large shear in a rotational diamond anvil cell: Simulation of loading, unloading, and reloading. *Comput. Mater. Sci.* 84, 404-416.
- Feng, B., Levitas, V. I., and Zarechnyy, O. M., 2013b. Plastic flows and phase transformations in materials under compression in diamond anvil cell: Effect of contact sliding. *J. Appl. Phys.* 114, 043506.
- Hemley, R.J., Mao, H.K., Shen, G.Y., Badro, J., Gillet, P., Hanfland, M., Hausermann, D., 1997. X-ray imaging of stress and strain of diamond, iron, and tungsten at megabar pressures. *Science* 276, 1242-1245.
- Jeanloz, R., Godwal, B.K., Meade, C., 1991. Static Strength and Equation of State of Rhenium at Ultra-High Pressures. *Nature* 349, 687-689.
- Javanbakht, M., Levitas, V. I., 2015. Interaction between phase transformations and dislocations at the nanoscale. Part 2. Phase field simulation examples. *J. Mech. Phys. Solids* 82, 164-185.
- Javanbakht, M., and Levitas, V. I., 2016. Phase field simulations of plastic strain-induced phase transformations under high pressure and large shear. *Phys. Rev. B* 94, 214104.
- Ji, C., Levitas, V.I., Zhu, H., Chaudhuri, J., Marathe, A., Ma, Y., 2012. Shear-Induced Phase Transition of Nanocrystalline Hexagonal Boron Nitride to Wurtzitic Structure at Room Temperature and Low Pressure. *P. Natl. Acad. Sci. USA*.
- Kilmametov, A.R., Khristoforova, A.V., Wilde, G., Valiev, R.Z., 2007. X-ray studies of nanostructured metals processed by severe plastic deformation. *Z. Kristallogr. Suppl.* 26, 339-344.

- Kim, K., Lambrecht, W.R.L., Segall, B., 1996. Elastic constants and related properties of tetrahedrally bonded BN, AlN, GaN, and InN. *Phys. Rev. B* 53, 16310-16326.
- Lang, J.M., Gupta, Y.M., 2011. Experimental Determination of Third-Order Elastic Constants of Diamond. *Phys. Rev. Lett.* 106.
- Levitas, V.I., 1996. *Large Deformation of Materials with Complex Rheological Properties at Normal and High Pressure*. Nova Science Publishers, New York.
- Levitas, V.I., 2004a. High-pressure mechanochemistry: Conceptual multiscale theory and interpretation of experiments. *Phys. Rev. B* 70, 184118.
- Levitas, V. I., 2004b. "Continuum mechanical fundamentals of mechanochemistry," in *High-pressure surface science and engineering*, edited by Y. Gogotsi and V. Domnich, Institute of Physics Pub, Bristol, Philadelphia, 159-293.
- Levitas, V. I., Ma, Y., Selvi, E., Wu, J., and Patten, J., 2012. High-density amorphous phase of silicon carbide obtained under large plastic shear and high pressure. *Phys. Rev. B* 85, 054114.
- Levitas, V. I., Ma, Y. Z., Hashemi, J., Holtz, M., and Guven, N., 2006. Strain-induced disorder, phase transformations, and transformation-induced plasticity in hexagonal boron nitride under compression and shear in a rotational diamond anvil cell: In situ x-ray diffraction study and modeling. *J. Chem. Phys.* 125, 044507.
- Levitas, V. I., and Javanbakht, M., 2015. Interaction between phase transformations and dislocations at the nanoscale. Part 1. General phase field approach. *J. Mech. Phys. Solids* 82, 287-319.
- Levitas, V. I., and Javanbakht, M., 2014. Phase transformations in nanograin materials under high pressure and plastic shear: nanoscale mechanisms. *Nanoscale* 1, 162-166.
- Levitas, V. I., Polotnyak, S. B. and Idesman A. V., 1996. Large elastoplastic strains and the stressed state of a deformable gasket in high pressure equipment with diamond anvils. *Strength Mater.* 28, 221-227.
- Levitas, V. I., and Zarechnyy, O. M., 2010a. Modeling and simulation of strain-induced phase transformations under compression in a diamond anvil cell. *Phys. Rev. B* 82, 174123.
- Levitas, V. I., and Zarechnyy, O. M., 2010b. Modeling and simulation of strain-induced phase transformations under compression and torsion in a rotational diamond anvil cell. *Phys. Rev. B* 82, 174124.
- Li, W. H., Yao, X. H., Branicio, P. S., Zhang, X. Q., Zhang N. B., 2017. Shock-induced spall in single and nanocrystalline SiC. *Acta Mater.* 140, 274-289.
- Lurie, A.I., 1990. *Nonlinear theory of elasticity*. Elsevier Science Pub. Co., New York.
- Manghnani, M.H., Katahara, K., Fisher, E.S., 1974. Ultrasonic Equation of State of Rhenium. *Phys. Rev. B* 9, 1421-1431.
- Murnaghan, F.D., 1951. *Finite deformation of an elastic solid*. Wiley, New York.
- Nagakubo, A., Ogi, H., Sumiya, H., Kusakabe, K., Hirao, M., 2013. Elastic constants of cubic and wurtzite boron nitrides. *Appl. Phys. Lett.* 102, 241909.
- Nielsen, O.H., 1986. Optical Phonons and Elasticity of Diamond at Megabar Stresses. *Phys. Rev. B* 34, 5808-5819.
- Novikov, N. V., Polotnyak, S. B., Shvedov, L. K., and Levitas, V. I., 1999. Regularities of phase transformations and plastic straining of materials in compression and shear on diamond anvils: experiments and theory. *J. Superhard Mater.* 3, 39-51.

- Nomura, R., Azuma, S., Uesugi, K., Nakashima, Y., Irifune, T., Shinmei, T., Kakizawa, S., Kojima, Y., Kadobayashi, H., 2017. High-pressure rotational deformation apparatus to 135 GPa. *Rev. Sci. Instrum.* 88, 044501.
- Razavi-Khosroshahi H., Edalati K., Arita M., Horita, Z. Fuji, M., 2016. Plastic strain and grain size effect on high-pressure phase transformations in nanostructured TiO<sub>2</sub> ceramics. *Scripta Mater.* 124, 59-62.
- Root, J.H., Small, W.M., Khatamian, D., Woo O.T., 2003. Kinetics of the  $\delta$  to  $\gamma$  zirconium hydride transformation in Zr-2.5Nb. *Acta Mater.* 51, 2041-2053.
- Rumyantsev, S. L., Levinshstein, M. E., Jackson, A. D., Mohammad, S. N., Harris, G. L., Spencer, M. G., and Shur, M. S., 2001. in *Properties of Advanced Semiconductor Materials GaN, AlN, InN, BN, SiC, SiGe*. Eds. Levinshstein M.E., Rumyantsev S.L., Shur M.S., John Wiley & Sons, Inc., New York.
- Saib, S., Bouarissa, N., 2009. Ab initio study of boron nitride at high pressures. *Diam. Relat. Mat.* 18, 1200-1204.
- Solozhenko, V.L., Elf, F., 1998. On the threshold pressure of the hBN-to-wBN phase transformation at room temperature. *J. Superhard Mater.* 20, 62-63.
- Srinivasarao, B., Zhilyaev, A. P., Perez-Prado, M. T., 2011. Orientation dependency of the alpha to omega plus beta transformation in commercially pure zirconium by high-pressure torsion. *Scripta Mater.* 65, 241-244.
- Todaka, Y., Sasaki, J., Moto, T., Umemoto, M., 2008. Bulk submicrocrystalline  $\omega$ -Ti produced by high-pressure torsion straining. *Scripta Mater.* 59, 615-618.
- Vohra, Y.K., Duclos, S.J., Ruoff, A.L., 1987. High-Pressure X-Ray-Diffraction Studies on Rhenium up to 216 GPa (2.16 Mbar). *Phys. Rev. B* 36, 9790-9792.
- Wang, K., Xiao, S., Deng, H., Zhu, W., Hu, W., 2014. An atomic study on the shock-induced plasticity and phase transition for iron-based single crystals. *Int. J. Plast.* 59, 180-198.
- Wang, K., Zhu, W., Xiao, S., Chen, K., Deng, H., Hu, W., 2015. Coupling between plasticity and phase transition of polycrystalline iron under shock compressions. *Int. J. Plast.* 59, 218-236.
- Wang, K., Chen, J., Zhu, W., Hu, W., Xiang, M., 2017. Phase transition of iron-based single crystals under ramp compressions with extreme strain rates. *Int. J. Plast.* 96, 56-80.
- Wills, R.R., 1985. Wurtzitic boron nitride - a review. *Int. J. High Technology Ceramics* 1, 139-153.
- Zhang, L., Li, Y. H., Cai, L.C. 2018. A formalism of two-phase equilibrium and phase diagram for elastic-plastic deformed system under non-hydrostatic stress conditions: Formulations and verification. *Int. J. Plast.* 104, 147-172.
- Zhilyaev A.P., Galvez F., Sharafutdinov A., Perez-Prado M.T., 2010. Influence of the high pressure torsion die geometry on the allotropic phase transformations in pure Zr. *Mater. Sci. Eng. A.* 527, 3918-3928.
- Zhilyaev, A. P., Sabirov, I., Gonzalez-Doncel, G., Molina-Aldareguia, J., Srinivasarao, B., Perez-Prado, M. T., 2011. Effect of Nb additions on the microstructure, thermal stability and mechanical behavior of high pressure Zr phases under ambient conditions. *Mat. Sci. Eng. A.* 528, 3496-3505.
- Zilbershtein, V.A., Chistotina, N.P., Zharov, A.A., Grishina, N.S., Estrin, E.I., 1975. Alpha-omega transition in titanium and zirconium during shear deformation under pressure. *Fiz.Met.Metalloved* 39, 445.